



1 **Organic vapors from Savannah and European Boreal fire emissions: Insights from**
2 **photochemical and dark aging experiments in a smog chamber**

3 Deeksha Shukla¹, Lejish Vettikkat², Mika Ihalainen³, Markus Somero³, Hendryk Czech^{*1},
4 Siegfried Schobesberger², Angela Buchholz², Iida Pullinen², Kerneels Jaars⁴, Kajar Köster³,
5 Viet Le⁵, Pasi Yli-Pirilä³, Stefan J. Siebert⁷, Pieter G. van Zyl⁴, Annele Virtanen², Ville
6 Vakkari^{4,5}, Olli Sippula^{3,6}, Ralf Zimmermann¹

7 ¹Chair of Analytical Chemistry, University of Rostock, Germany

8 ²Department of Technical Physics, University of Eastern Finland, Kuopio, Finland

9 ³Department of Environmental and Biological Sciences, University of Eastern Finland, Kuopio, Finland

10 ⁴Atmospheric Chemistry Research Group, Chemical Resource Beneficiation, North-West University,
11 Potchefstroom, South Africa

12 ⁵Finnish Meteorological Institute, Helsinki, Finland

13 ⁶Department of Chemistry and Sustainable Technology, University of Eastern Finland, Joensuu, Finland

14 ⁷Unit for Environmental Sciences and Management, North-West University, Potchefstroom, South Africa.

15

16 *Correspondence to:* Hendryk Czech (hendryk.czech@uni-rostock.de)

17

18 **Abstract**

19 Biomass burning (BB) emits large amounts of pollutants in the particle and gas phases, with significant
20 implications for air quality, human health and climate. Here, we investigate the emission of organic vapors from
21 controlled burns of relatively understudied biomass fuels: woody plants and grasses from African savannah and
22 European boreal forest surface using a high-resolution proton transfer reaction-mass spectrometer. To understand
23 the effect of different oxidation regimes, organic vapors were aged in a 29 m³ Teflon chamber, where
24 photochemical and dark aging were simulated. The average total primary emission factors (EFs) for organic vapors
25 varied considerably with fuel type, ranging from 69 to 161 g kg⁻¹. Photochemical aging led to substantial depletion
26 of furanics, phenolics and oxygenated aromatics, accompanied by enhancements of carbonyl B compounds and O-
27 containing compounds C<6 across experiments. In contrast, dark aging under low-NO_x conditions produced
28 minimal compositional changes. Hierarchical clustering of relative composition showed clear regime dependence,
29 with regime-associated differences accounting for 73% of the variance in group-level composition. Toluene and
30 furan showed a strong negative correlation with secondary oxygenated volatile organic compounds (OVOCs),
31 including anhydrides and small acids, consistent with their role as precursors. After 0.5 equivalent day of
32 photochemical aging, organic vapors shifted to higher O/C (>0.70) and an increased fraction of C_xH_yO_z (z≥3).
33 These results highlight the integral role of OH·-driven photo-oxidation in governing the atmospheric evolution and
34 composition of BB organic vapors and underscore the need for secondary organic aerosols (SOA) models to
35 include non-traditional precursors.

36

37

38



39 1 Introduction

40 Biomass burning (BB), including forest and savannah fires, is a major source of atmospheric aerosols and trace
41 gases in the atmosphere (Andreae, 2019) and is considered the second largest global source of organic vapors
42 (Akagi et al., 2011; Yokelson et al., 2008). BB emissions not only have significant impacts at local or regional
43 scales but also may affect global atmospheric chemistry (Lewis et al., 2013) and Earth's climate (Keywood et al.,
44 2013; Stocker et al., 2021). Organic vapors from BB emissions contain many oxygenated compounds and undergo
45 further oxidation in the atmosphere, producing a mixture of products spanning a broad range of volatility (Koss et
46 al., 2018). Low-volatile oxidation products partition into the condensed phase, form secondary organic aerosols
47 (SOA) and may enhance cloud condensation nuclei (CCN) activity (Calvert et al., 2002; Kroll & Seinfeld, 2008;
48 Pospisilova et al., 2020). Furthermore, the large amounts of NO_x and reactive organic vapors co-emitted from BB
49 have the potential to form tropospheric O₃, which can be transported over large distances (Jaffe & Wigder, 2012;
50 McKeen et al., 2002; Pfister et al., 2008; Vakkari et al., 2020). Emission of these organic vapors from BB varies
51 significantly depending on factors such as biomass fuel, combustion conditions, fuel-moisture content, burning
52 phase, time of the day and other variables (Chen et al., 2010; Czech et al., 2017; Rivera-Adorno et al., 2025;
53 Sekimoto et al., 2018; Vakkari et al., 2018). Global warming has increased the frequency, intensity and behavior
54 of wildfires in recent decades, making wildfires an important source of atmospheric pollution over time (Rogers
55 et al., 2020). The long-range transport of wildfires from northern boreal regions like Siberia is known to affect the
56 radiative balance and aerosol composition in the sensitive ecosystem of the Arctic region (Cali Quaglia et al., 2022;
57 Schneider et al., 2024). Moreover, long-range transport of wildfire emissions in Canada substantially decreased
58 the air quality in metropolitan areas of the US East Coast (Kolden et al., 2024).

59 In recent years, wildfire activity has intensified in Europe, with the continent recording its second-largest burned
60 area in 2022 (EU-JRC, 2023) and approximately 500,000 ha burnt in 2023 (San-Miguel-Ayanz et al., 2023), which
61 was the largest individual wildfire ever mapped in Europe. The impacts and severity of wildfires are expected to
62 grow in response to climate change (Whitman et al., 2019). To understand the impact of wildfire emissions better,
63 BB emissions have been extensively investigated either by field experiments (Brito et al., 2014; Garofalo et al.,
64 2019; Gkatzelis et al., 2024; Hobbs et al., 2003; Liang et al., 2022a; Vakkari et al., 2014; Warneke et al., 2023)
65 and/or by simulating natural fire in a laboratory (Ahern et al., 2019; Akherati et al., 2020; Fang et al., 2021; Gilman
66 et al., 2015). However, fewer studies (Hobbs et al., 2003; Sinha et al., 2003; Swap et al., 2003) exist related to
67 savannah fire emissions and their aging despite their significant contribution to the global aerosol burden. Boreal
68 BB emissions, acknowledged as a crucial contributor to Arctic climate change (Zhong et al., 2024), are rarely
69 explored in European boreal forest surface fires compared to North American boreal forest (Boby et al., 2010;
70 Zhao et al., 2021).

71 The atmospheric evolution of the BB plume is a complex process and is affected by various factors like
72 heterogeneous chemistry and plume dilution. Functionalization or oligomerization reactions produce low volatility
73 gas-phase species that gradually condense to form SOA; however, continued oxidation makes fragmentation
74 reactions dominate resulting in lower SOA yields (Kroll et al., 2009; Lambe et al., 2012). Plume-dilution can cause
75 condensed semi-volatile compounds to evaporate, reducing the organic loading (Pagonis et al., 2023; Palm et al.,
76 2020). These evaporated compounds may recondense after further oxidation, continuously altering the composition
77 and properties of organic vapors (Akagi et al., 2012; Garofalo et al., 2019; Mason et al., 2001). The co-existence
78 of primary emission and secondary formation products adds complexity to the evolution, making characterization



79 of organic vapors critical. There exists a discrepancy between ambient wildfire plumes and those aged in laboratory
80 smog chambers when it comes to net secondary organic aerosol (OA) formation with aging, smog chamber studies
81 generally indicating stronger SOA formation (Hodshire et al., 2019).

82 Over the past decades, field and chamber studies have investigated the oxidation of BB emissions during either
83 daytime, driven by OH[·], or nighttime, driven by NO₃[·] and O₃ (Czech et al., 2024; Georgopoulou et al., 2025;
84 Hodshire et al., 2019; Kodros et al., 2020; Tkacik et al., 2017; Yazdani et al., 2023). However, NO₃[·] chemistry can
85 also be relevant during daytime due to suppressed photolysis in optically thick plumes (Decker et al., 2021). These
86 atmospheric aging processes are likely to substantially alter the key properties of BB emissions with respect to
87 climate and health. As BB plumes age, rapid oxidation of non-methane hydrocarbons (NMHCs) produces a
88 complex mixture of oxygenated volatile organic compounds (OVOCs). Since the atmospheric oxidizing capacity
89 is largely controlled by OH[·], and OVOC photolysis is a major OH[·] source (Wolfe et al., 2022), OVOCs exert
90 significant impacts on tropospheric photochemistry (Dai et al., 2025). Simultaneously, several OVOCs,
91 particularly carbonyls, pose a threat to human health and have been associated with cytotoxic, mutagenic, and
92 carcinogenic effects (Marques et al., 2021; Stabbert et al., 2017). Furthermore, the role of VOCs (Ahern et al.,
93 2019; Akherati et al., 2020) and more recently, of semi-volatile or intermediate-volatility organic compounds
94 (S/IVOCs) as key gas-phase precursors in SOA formation has been extensively investigated. A recent study (Li et
95 al., 2024a) reported that IVOCs accounted for ~70% of the total SOA, more than twice the contribution from
96 VOCs, providing the first direct evidence on their central role and advancing our understanding of the chemical
97 drivers of SOA formation. However, the chemical complexity of organic vapors from BB emissions, along with
98 analytical limitations, continues to pose challenges for detailed identification and quantification of a diverse range
99 of species. As a result, there remains a limited understanding of major organic vapors from BB emissions, their
100 evolution and the effects of atmospheric aging on them. Furthermore, since BB emissions are ensembles of
101 complex organic compounds, their collective reactivity often differs from that of individual species. This makes it
102 important to investigate their behavior through bulk molecular-level characterization, which can offer valuable
103 insights into their atmospheric dynamics.

104 Advancements in analytical instrumentation have significantly improved our ability to characterize the molecular-
105 level composition of organic vapors. Traditionally, gas chromatography (GC) and multidimensional GC coupled
106 with mass spectrometry (GC-MS) have been widely used to measure selected VOCs and NMHCs (Lewis et al.,
107 2000). While these offline analytical techniques remain indispensable for analyzing specific compounds, they are
108 limited by their focus on a narrower subset of analytes, extensive sample preparation/analyses times and potential
109 for artifacts. Proton-transfer-reaction mass spectrometry (PTR-MS) emerged as a sophisticated technique for real-
110 time detection of a broad range of volatile compounds with high sensitivity without pre-concentration or separation
111 (Hansel et al., 1995; B. Yuan et al., 2017a). Subsequent integration with high-resolution time-of-flight analyzers
112 (PTR-TOF-MS) expanded its analytical ability with higher mass-resolution and response time, thereby enabling
113 the detection of lower-volatility compounds and highly oxygenated species (Bruns et al., 2017; Koss et al., 2018).
114 High resolving power TOF-MS allows separation of compounds that are isobaric at unit mass resolution and
115 enables molecular formula assignment, however, without an additional separation dimension (e.g. retention time),
116 it cannot distinguish isomers that share the same chemical formula (Hatch et al., 2017). One option to improve the
117 selectivity of PTR(-TOF)-MS analyses is to switch between different reagent ions (H₃O⁺, NH₄⁺, NO⁺, O₂⁺), which
118 enhances sensitivity towards different compound classes (Reinecke et al., 2023), although in practice such



119 switching must be sufficiently fast to capture rapid change in emissions, so hyper-fast GC (Gehm et al., 2021)
120 offers an alternative route to separate and track dynamic changes in emissions while maintaining a reasonable time
121 resolution. More recently, Vocus PTR-TOF-MS has introduced several technical innovations over earlier-
122 generation PTR systems, most notably a redesigned chemical ionization source that substantially enhances ion
123 transmission efficiency, resulting in higher detection of product ions (Krechmer et al., 2018). This advancement
124 has expanded its detection capabilities for a wider range of VOCs, IVOCs and their oxidation products, such as
125 monoterpene oxidation products with up to six oxygen atoms (Li et al., 2020)

126 In this study, we use a Vocus PTR-TOF-MS to elucidate how different oxidation regimes affect the emission of
127 organic vapors from three globally relevant, yet relatively under-studied biomass fuels i.e. European boreal forest
128 surface samples collected in Finland, and woody plants and grasses sourced from a grassland savannah
129 environment in South Africa. We begin by discussing the characteristics of primary organic vapor emissions for
130 each biomass fuel. We then examine how these organic vapors evolve and how their chemical composition
131 transforms under simulated photochemical and dark aging in a smog chamber to highlight the atmospheric
132 relevance of the results. High-resolution, real-time measurements of organic vapors from such understudied
133 biomass sources are essential for advancing our current understanding of BB contributions to the global aerosol
134 burden and associated environmental and climate impacts.

135 2 Material and methods

136 2.1 Fuels and Biomass-burning (BB) experiments

137 The experiments were conducted under the framework of the boreal and savannah fire aerosol aging (BASFAA)
138 campaign that took place at the ILMARI facility in the University of Eastern Finland, Kuopio, Finland, during
139 May-June 2022. Laboratory burns of three different biomass fuels, i.e. boreal forest surface from Finland, woody
140 and grassy material from the savannah in South Africa, were performed. European boreal forest surface samples
141 (including vegetation, litter and soil organic horizon) were collected from the Evo experimental fire area (Köster
142 et al., 2024), located in an even-aged 75-year-old Scots pine stand, while woody plants and grasses were collected
143 from a grassland savannah environment near the Welgegund atmospheric measurement station (Jaars et al., 2016)
144 in South Africa. Further details of each biomass, including moisture, carbon content etc., are documented in a
145 previous publication focused on primary emission characterization (Vakkari et al., 2025).

146 Combustion was conducted under an open-stack setup designed to mimic natural burning and dilution conditions,
147 following the approach by (Christian et al., 2003) but on a smaller scale with fuel bed diameter of approx. 50 cm
148 where a 6 cm in diameter sample holder was placed for the savannah biomasses. For boreal forest surface the
149 sample holder was 23 cm in diameter. Combustion was conducted as batch burns where a pre-weighed fuel load
150 (typically 50-60 g for savannah fuels and ~500 g of boreal forest surface was placed on the fuel bed and ignited
151 using a resistor heating element. Before each experiment, a continuous flow of zero air (Adco Instruments Inc.,
152 Model 737-250), was used to flush the smog chamber and sampling lines through lines to prevent cross-
153 contamination between burns and to maintain a low VOC background. The sample was introduced from the stack
154 into a 29 m³ smog chamber (Leskinen et al., 2015) via a two-stage dilution-system comprising of a porous tube
155 diluter followed by an ejector diluter (Dekati, Type, Finland). The smog chamber is a collapsible Teflon bag
156 chamber equipped with 47 blacklight lamps (354 nm, Sylvania F40 W/350 BL) (Leskinen et al., 2015). The relative
157 humidity inside the chamber was maintained at 20% for savannah grass and savannah wood experiments and 50%
158 for boreal forest surface experiments using a humidification setup described in Leskinen et al. (2015). The



159 instrumentation layout at the ILMARI facility was similar to as described in Tiitta et al. (2016). Detailed
160 description of the experimental design and associated instrumentation are provided in Vakkari et al. (2025).

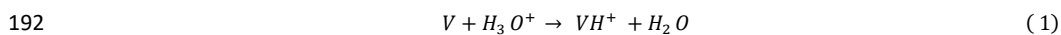
161 2.2 Aging procedure in smog-chamber

162 After injection into the chamber and thorough mixing, a 45-minute period of primary measurements was made.
163 After primary measurements, oxidant (O_3) was injected into the chamber and aging experiments were conducted
164 in both photochemical and dark conditions. In dark aging experiments, only O_3 was injected, while in
165 photochemical aging experiments, along with O_3 , UV-lights were switched on and additional H_2O_2 was added into
166 the chamber to generate $OH\cdot$. Initial O_3 concentration was approximately 50 ppb for photochemical aging
167 experiments and 100 ppb for dark aging experiments. The $OH\cdot$ exposure in the chamber was traced by injecting
168 butanol-d9 and monitoring its decay during experiments (Barnet et al., 2012). A butanol-d9 reaction rate
169 coefficient of $3.4 \times 10^{-12} \text{ cm}^3 \text{ molecule}^{-1} \text{ s}^{-1}$ at 295 K was assumed (Allani et al., 2021). The extent of photochemical
170 age is discussed in terms of equivalent (eqv.) day as 24 hours spent at the average ambient $OH\cdot$ concentration of
171 $1.5 \times 10^6 \text{ molecules cm}^{-3}$. In the dark aging experiments, NO_x concentrations in the chamber were low, and under
172 these low- NO_x (<10 ppb) conditions, formation of $NO_3\cdot$ is expected to be limited, so dark aging was largely driven
173 by O_3 . The O_3 exposure was calculated by O_3 concentrations integrated over time, and then the ambient O_3
174 concentration of $7 \times 10^{11} \text{ molecule cm}^{-3}$ (Ziemann & Atkinson, 2012) was used to convert the exposure into eqv.
175 atmospheric day for dark aging experiments. Details of the 21 experimental burns used in the organic vapor
176 analysis (savannah grass, n=9; savannah wood, n=7; boreal forest surface, n= 4; blank experiment, n=1), including
177 modified combustion efficiency (MCE), fuel type and aging condition are provided in supplementary information
178 (Table S1).

179 For primary measurements, data were averaged over a 30-minute period before the addition of oxidant, and for
180 aging experiments, averaged over the time interval corresponding to 0.5 eqv. day of atmospheric aging for all
181 experiments, providing a standardized reference point for comparing aging experiments conducted on different
182 days. In photochemical aging experiments, time-zero is referred to as the moment when UV lights were switched
183 on, whereas in dark aging experiments, it's when O_3 was injected in the chamber.

184 2.3 Measurements and analysis of organic vapors

185 The VOC measurements were conducted using a Vocus PTR-TOF-MS (Tofwerk AG, Aerodyne Research Inc;
186 Krechmer et al., 2018) (hereinafter referred to as PTR-MS). VOCs with proton affinity greater than that of water
187 are ionized by the primary ion H_3O^+ to form protonated VOC ions. Most VOCs can be detected using this
188 technique. However, small alkanes, ethene and ethyne with low proton affinities remain undetected by PTR-MS.
189 While the proton affinities of larger alkanes increase with molecular size (Fu et al., 2022), their ionization remains
190 inefficient, and detection is compromised by extensive fragmentation (Gueneron et al., 2015). The proton transfer
191 reaction for a VOC, V can be expressed as in Equation 1:



193 This PTR-MS has a focusing ionization molecule reactor (FIMR), which can focus the ions to the central axis,
194 reducing the detection loss and thereby increasing the sensitivity. An additional advantage is that the water mixing
195 ratio inside the FIMR is >15 % v/v, and hence there is no humidity dependence on the sensitivity. The drawback
196 is that a quadrupole low-mass filter is used to reduce the primary ions reaching and degrading the MCP, hence



197 normalization is not possible, and regular calibrations are needed. The transmission of m/z below 50 is also
198 compromised.

199 The PTR technique is generally regarded as a soft ionization technique compared to electron impact ionization.
200 However, the $[RH]^+$ ions generated (Equation 1) can fragment inside the reactor due to the added energy from the
201 exothermic protonation reaction and collisions (Li et al., 2022a; Gueneron et al., 2015). Higher collision energy
202 tends to suppress the water clustering of both reagent and product ions; however, it can also promote fragmentation
203 of protonated ions (Li et al., 2022a). In this study, PTR-MS FIMR was operated at 2.5 mbar pressure, 100 °C
204 temperature and an electric field strength of 57.5 V cm⁻¹, resulting in the field strength of 118.5 Townsend (10⁻¹⁷
205 V cm²). These conditions were selected to achieve a balance so that excessive formation of water-cluster ions was
206 avoided while maintaining stable protonated analyte ions with limited fragmentation. For α -pinene, the measured
207 ion signals were distributed at m/z 81 (49%) and m/z 137 (51%), which was in line with a previous study (Simon
208 et al., 2023). Fragmentation however was not accounted for individual ions, therefore compound-dependent
209 fragmentation may cause over- or underestimation of the mixing ratios for certain molecular ions.

210 The chamber air was sampled into the PTR-MS through a 3 m long polytetrafluoroethylene (PTFE) tubing (6mm
211 O.D, 5mm I.D.) with an extra flow of 3 lpm. The PTR-MS was operated at 1 Hz and was averaged to a working
212 time resolution of 10 seconds. The PTR-MS data were recorded in Hierarchical Data Format version 5 (HDF5)
213 using software called TofDaqRec. These raw data files were analyzed using the MATLAB-based tofTools R612
214 (Junninen et al., 2010), where custom peak shape determination, mass calibration, resolution function
215 determination, and high-resolution peak fitting were performed. The mass transmission function and the ratios of
216 measured and calculated sensitivities for a series of ions were used for data-quantification and conversion of ion-
217 counts to parts per billion by volume (ppbv). The PTR-MS during the campaign had a mass accuracy of <5ppm
218 with a mass resolving power of ~10000 Th/Th.

219 Regular automated single-point calibrations (n=80) were performed using a gas mix of 14 calibration standards
220 (Apel Reimer Environmental Inc.). The compounds calibrated with the standards were ethanol, acetonitrile,
221 acetone, acrylonitrile, isoprene, methyl vinyl ketone (MVK), methyl ethyl ketone (MEK), benzene, m-xylene, α -
222 pinene, 1,2,4-trimethylbenzene, siloxanes (D4 and D5) and β -caryophyllene. The calibration gas contained
223 approximately 1 ppmv (except for β -Caryophyllene at 100 ppbv) and was diluted with zero air from the zero-air
224 generator (Tofwerk AG) to achieve a target mixing ratio of 4 ppbv for the single-point calibrations. Limits of
225 detection (LODs) for the 14 calibrants were estimated from background measurements as the 3 σ (at 10 s) and are
226 presented in supplementary information (Table S2). The maximum sensitivity was observed for acetone and was
227 used as the sensitivity factor for calibrating all non-calibrant ions. Hence, the reported ppbv values represent lower
228 limits. To calculate uncertainties in instrument precision, uncertainties in VOC calibration gas mixing ratio (5%)
229 and in the MFCs used for dilution (1% each) were used. An uncertainty of 7.2% resulted for acetone. Thus, the
230 uncertainty in the total VOC concentration from the PTR-MS is estimated to be 10%, in agreement with (Jensen
231 et al., 2023). The instrument zeros were done regularly for 30 seconds every 15 minutes. The zeros were linearly
232 interpolated and subtracted from the measured data.

233 All detected and identified ions (n=436) except the primary ions (H₂O)_nH⁺, and ions containing deuterated hydrogen
234 (²H), water clusters, silicon (Si) and fluorine (F) were used for further analysis. Approximately 61% of the total
235 organic vapor mass measured using the PTR-MS was assigned.

236



237 **2.4 Data processing and Quantification**

238 MCE as a function of time was calculated from primary flue-gas CO₂ and CO concentrations as per (Akagi et al.,
239 2011). The emission factors (EFs; g kg⁻¹ fuel) of species *i* were calculated following a carbon mass balance
240 approach (Yokelson et al., 1999) as per Equation 2:

241

$$242 \quad EF_i \left(\frac{g}{kg} \right) = F_c \times 1000 \times \frac{MW_i}{12} \times \frac{ER_i}{\sum_{j=1}^n \frac{C_j}{\Delta CO}} \quad (2)$$

243

244 Here, EF_{*i*} refers to the mass (g) of species (*i*) emitted per mass (kg) of dry fuel burned, F_{*c*} is the fuel carbon fraction,
245 MW_{*i*} is the molecular weight of the species (*i*), ER_{*i*} is the emission ratio of species (*i*) with respect to ΔCO, and C_{*j*}
246 is the number of moles of carbon for species (*j*). In the summation, carbon emitted as CO₂, CO, CH₄, VOCs, OC,
247 and BC is included (Vakkari et al., 2025). For each species, background concentration before sample injections
248 has been subtracted. F_{*c*} was 48.8% for savannah wood, 43% for savannah grass and 42.8% for boreal forest fuel
249 (Vakkari et al., 2025).

250 Outlier detection was performed using Hampel filter (median ± median absolute deviation) for each detected ion,
251 and at each time step, a robust z-score was computed as the absolute deviation from the local median divided by
252 1.4826×MAD. Points with a robust z-score larger than a threshold (k ≈ 5) were flagged as candidate spikes. Isolated
253 spikes were removed only when they occurred as short excursions (<3 points); longer changes were retained as
254 real variability. A total of 436 measured molecular ions were then classified according to their functional groups
255 into 11 major classes (Table S3) similar to previous combustion studies (Bhattu et al., 2019; Hartikainen et al.,
256 2024; Wang et al., 2025). These classes include hydrocarbons (C_{*x*}H_{*y*}), aromatic hydrocarbons (ArHCs) including
257 single ring aromatics and polycyclic aromatic hydrocarbons, oxygenated aromatic, furanic, O-containing
258 compounds containing C<6 and C≥6, CHN and CHNO, phenolic and carbonyl compounds. Carbonyl compounds
259 were classified into carbonyl A and carbonyl B by analyzing their emission trends during the photochemical aging
260 experiments. For each compound, a robust Theil-Sen estimator was used to calculate the slope of its EF over the
261 ageing period across biomass type. Compounds with ≥80% experiments showing a negative slope (decreasing
262 trend) were assigned to carbonyl A, while those with a positive slope (increasing trend) were assigned to carbonyl
263 B. The molecular formulas assigned to each compound class are provided in Table S3 in supplementary
264 information.

265 The degree of unsaturation of detected ions was estimated using double bond equivalents (DBE) which describes
266 the total amount of double bond and ring structures in the molecule. DBE values were calculated as per Equation
267 3:

$$268 \quad DBE = C - \frac{H}{2} + \frac{N}{2} + 1 \quad (3)$$

269 Here, C, H, N represent the number of carbons, hydrogen, and nitrogen present in the molecules, respectively.

270 Mass defect plots for organic vapors were used further to visualize the difference in mean mixing ratio of
271 compounds between fresh and aged emissions and to highlight dominant signals present for each fuel and aging
272 condition. Compounds were further classified into elemental classes such as C_{*x*}H_{*y*}, C_{*x*}H_{*y*}N_{*i*}, C_{*x*}H_{*y*}O (z < 3), C_{*x*}H_{*y*}O_{*z*}
273 (z ≥ 3), and C_{*x*}H_{*y*}O_{*z*}N_{*i*} where *x*, *y*, *z* and *i* denote the numbers of carbon, hydrogen, oxygen and nitrogen atoms,
274 respectively. Marker sizes were scaled to the relative mean mixing ratio within each class.



275 2.5 Statistical analysis

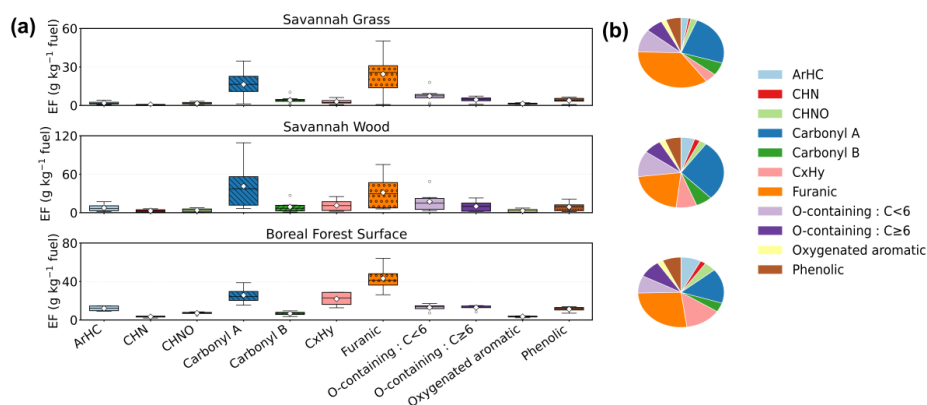
276 A cluster map (hierarchically clustered heatmap) was used to visualize relationships between samples and
277 compound groups, using the SciPy library in Python 3.9. The cluster map shows group-level mean mixing ratios
278 aggregated by compound group (rows) and oxidation regime-resolved samples (columns; date x fuel x regime).
279 Group means were standardized by sample (column; z scored within each sample across groups), so the associated
280 heatmap displays how many standard deviations a given compound group lies from that sample's mean, indicating
281 relative enrichment/depletion of compound groups within each sample. Dendrograms obtained with Euclidean
282 distances and Ward's minimum-variance algorithm (Nguyen et al., 2021) illustrate similarity among compound
283 groups and among samples (date x fuel x regime). MCE was included as a continuous annotation track to aid
284 interpretation but was not used to compute clustering distances. Tree fidelity was assessed with the cophenetic
285 correlation coefficient, which measures the agreement between dendrogram heights and the underlying distance
286 matrix, and is interpreted similarly to Pearson's correlation coefficient (Sokal & Rohlf, 1962). Multivariate
287 comparisons were performed in the same space used for the cluster map i.e. standardized sample x group matrix.
288 One-way Permutational Multivariate Analysis of Variance (PERMANOVA) (Anderson, 2001, 2017). Euclidean
289 distance matrices were used to quantify how much of the variance in composition was associated with regime
290 (fresh, O₃, UV+O₃), fuel (savannah grass, savannah wood, boreal forest surface), and to test regime effects within
291 each fuel. For each model, pseudo-F statistic, R² (proportion of variance explained), and p-value were obtained
292 from 999 permutations of the sample labels.
293 To assess whether the differences in composition were related to MCE, a Mantel test (Spearman) was additionally
294 performed between the Euclidean composition distance matrix and a distance matrix of pairwise |ΔMCE|, using
295 999 permutations to assess significance.

296

297 3 Results and Discussion

298 3.1 Primary gaseous organic emissions

299 A total of 436 ions were identified based on the elemental composition derived from MS and were then classified
300 into 11 major classes using formula-based functional-group assignments. The average MCE during batch
301 combustion were between 0.59 to 0.97. The EFs of organic vapors varied based upon the biomass fuel type and
302 MCE values, and generally lower MCE values corresponded to higher EFs of organic vapors, excluding two
303 glowing-phase experiments with low EFs values (Vakkari et al., 2025). Under low-MCE and low-temperature
304 conditions, organic vapor emissions are likely dominated by primary pyrolysis products of biomass (Akagi et al.,
305 2011). However, combustion under low-MCE conditions generally proceeds at a lower burn rate than flaming
306 combustion. Thus, despite higher EFs, the mass of emitted pollutants after a certain time interval is typically larger
307 for flaming combustion. The total EFs for the gaseous organic compounds had an average (standard deviation)
308 value of 69 (21), 147 (53) and 161 (22) g kg⁻¹ fuel burnt for savannah grass, savannah wood and boreal forest
309 surface across all the experiments. The average total EFs for each fuel were relatively higher than the total average
310 EFs reported from previous studies, however, the number of ions considered in this study was approximately 3–4
311 times higher than in previous studies (Gkatzelis et al., 2024; Koss et al., 2018; Permar et al., 2021; Travis et al.,
312 2023). Figure 1 shows EFs for each of the classes in a box-and-whisker plot, highlighting the distributional
313 behavior with median and interquartile ranges (IQR) reported for each fuel x class in supplementary information
314 (Table S4).



315

316 **Figure 1.** (a). Fresh emission factors (EFs) distributions by compound class for savannah grass, savannah wood,
 317 and boreal forest surface. For each fuel, boxplots show the variability across experiment days of class-averaged
 318 EFs (g kg⁻¹ fuel). Boxes are colored by class (ArHC, CHN, CHNO, carbonyl A, carbonyl B, C_xH_y, furanic, O-
 319 cont.: C<6, O-cont.: C≥6, oxygenated aromatic, phenolic). Boxplots use 1.5×IQR whiskers; hollow circles =
 320 outliers; white diamonds = mean. (b) Companion pie charts showing the mean fractional contribution (%) of each
 321 class to the total Fresh EF for the same fuels.

322 Fresh emissions were dominated by small oxygenate species like furanic, carbonyl A and O-containing compounds
 323 with C<6. Savannah wood exhibited the most variable fresh EFs across the classes, with a median value of 37.4 g
 324 kg⁻¹ fuel (IQR 56.2-11.7) for carbonyl A, which can be attributed to highest variability in MCE for savannah wood
 325 experiments (0.59-0.95) compared to MCE ranges in savannah grass (0.76-0.97) and boreal forest surface (0.74-
 326 0.84) experiments. Savannah grass showed the lowest overall emissions with furanic compounds dominating the
 327 emissions with a median value of 25.7 g kg⁻¹ fuel (IQR 30.9-13.8). The differences in emissions largely reflected
 328 variations in MCE across the biomass fuels. In particular, the glowing combustion cases for savannah grass
 329 contributed to its lower overall EFs.

330 Boreal forest surface biomass fuel showed high EFs of hydrocarbons (C_xH_y) with a median value of 23.0 g kg⁻¹
 331 fuel (28.7-16.2), which was 2-fold and 10-fold higher than the median C_xH_y from savannah wood and savannah
 332 grass, respectively. The relative contribution of individually measured chemical classes to the total EF is shown in
 333 Figure 1b. Carbonyl A and furanic compounds alone contributed to the major fractions of total primary emission,
 334 especially for savannah fuels (59% for savannah grass and 49% for savannah wood). Carbonyl compounds are key
 335 precursors for atmospheric organic acids and strongly facilitate the formation of SOA (Liu et al., 2022). They can
 336 be formed as intermediate gaseous oxidation products when certain VOCs react with atmospheric oxidants, and
 337 because some of these carbonyls are relatively water-soluble, they can dissolve into the aqueous aerosol phase and
 338 undergo further particle-phase reactions, e.g., oligomer formation of α-dicarbonyls (Kawamura et al., 2013). Furan
 339 and their derivatives, acknowledged as ‘non-traditional SOA precursors’, have been identified as predominant
 340 species in BB emissions and gained attention in recent years (Bruns et al., 2017; Hartikainen et al., 2018; Li et al.,
 341 2024b; Müller et al., 2016). A study by Coggon et al., 2019 also suggested furans as significant precursors of
 342 secondary organic vapors measured by PTR-TOF-MS and other chemical ionization mass spectrometers and shed



343 light on the importance of furan chemistry in biomass burning plumes. In this study, OVOCs such as carbonyls,
344 furanic, O-containing compounds, oxygenated aromatics and phenolic compounds form the major fraction of
345 emissions, i.e. >89% and >82% for savannah grass and savannah wood and >72% for boreal forest surface,
346 respectively. Previous studies have also found oxygenated species to be a large portion of organic vapor emissions
347 across various biomass fuels (Bruns et al., 2016; Gilman et al., 2015; Koss et al., 2018; Stockwell et al., 2015; Zhu
348 et al., 2021). These OVOCs have important atmospheric implications as their photolysis is an important source of
349 HO_x, which promotes NO-to-NO₂ recycling and thereby drives O₃ production via NO₂ photolysis (Li et al., 2022b).
350 OVOCs were also found to be a more important source for BB-derived SOA than heterocyclics, especially at lower
351 (<1 day) aging times (He et al., 2024).

352 OVOCs were followed by C_xH_y (4-8%) for savannah grass and savannah wood, whereas the C_xH_y fraction was
353 higher for boreal forest surface (14%). ArHCs contributed a smaller fraction (3-5%) for savannah grass and
354 savannah wood but were higher (7%) for boreal forest surface. Previous airborne observation of boreal wildfire
355 plumes reported a hydrocarbon-rich organic vapor composition, with hydrocarbons contributing ~53% of the total
356 measured organic vapors (Hayden et al., 2022). Nitrogen-containing compounds together had ~3-5% contributions
357 to total primary organic vapor emission for savannah fuels and ~7% contribution for boreal forest surface. Phenolic
358 compounds contributed 6-7% to the total primary organic vapor EFs across the fuels. Phenolic compounds are
359 considered as important OH· reactants for the formation of secondary brown carbon formation in BBSOA (Palm
360 et al., 2020). Several dominant compounds were identified based on their contribution to the total EFs across the
361 primary experiments, e.g. furfural (C₅H₄O₂; 1.4-12.9%), 4-methoxy-2(5H)-furanone (C₅H₆O₃; 0.8-7.1%), acetic
362 acid (C₂H₄O₂; 1.8-12.5%), acetic anhydride (C₄H₆O₃; 1.5-5.6%), acetone (C₃H₆O; 1.7-5.1%), hydroxy acetone
363 (C₃H₆O₂; 1.5-6.1%), C₂H₆O₃ (3.7-17.8%). Many of these compounds were also reported in previous BB studies
364 (Bruns et al., 2017; Stockwell et al., 2015; Wang et al., 2025).

365 3.2 Chemical evolution of organic vapors in the chamber

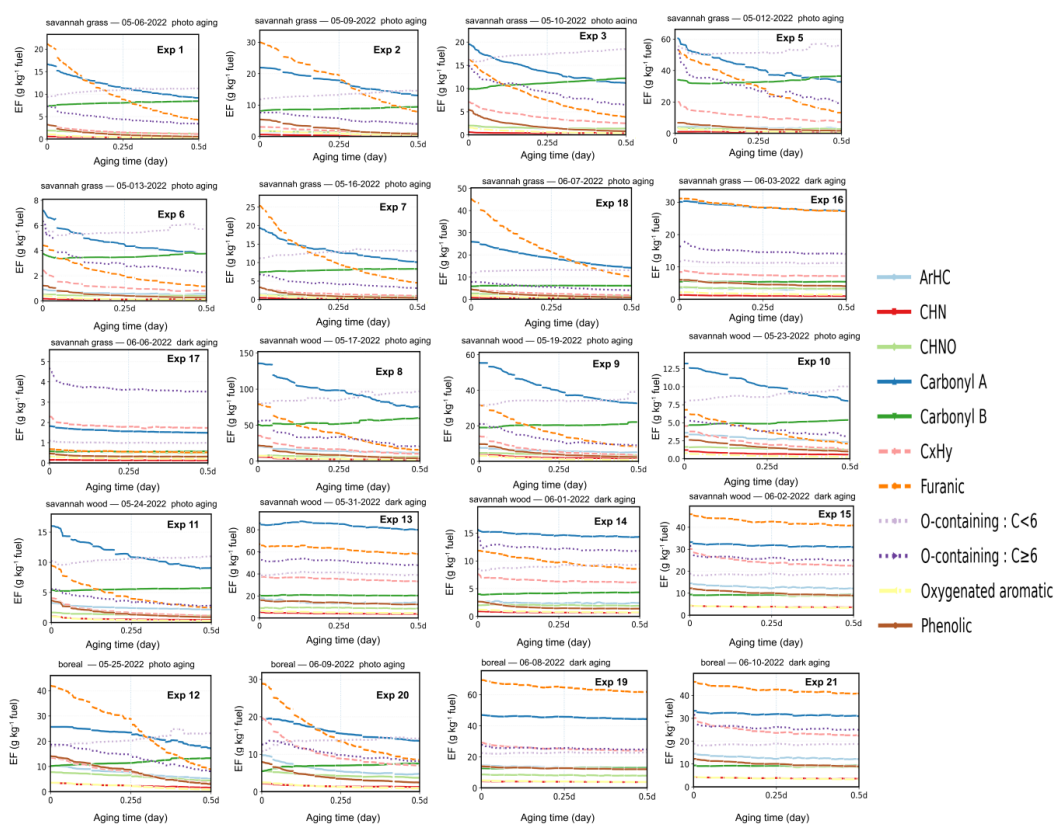
366 The evolution of organic vapors classified by functional group classes with eqv. day of aging (standardized to 0.5
367 eqv. day of aging) for both photochemical and dark aging experiments for savannah grass, savannah wood and
368 boreal forest surface biomass fuel is shown in Figure 2.

369 At time zero (t=0h), UV lights were turned on for daytime photooxidation with OH· acting as a dominant oxidant,
370 and behavioral changes of each class were observed. In general, OH· reacts with VOCs via three main pathways,
371 including H-atom abstraction, and OH· addition to C=C bonds and aromatic rings, which accelerate the depletion
372 of unsaturated and aromatic classes and drives the formation of more oxygenated products (Ziemann & Atkinson,
373 2012). During the photochemical aging experiments, the most extensive decay was observed for furanic, phenolic
374 and oxygenated aromatic compounds across the biomass fuels. Furanic compounds especially showed rapid decay
375 immediately after the UV lights were switched on, consistent with fast processing driven by OH· oxidation and
376 potential additional loss via direct photolysis. Furan aldehydes exhibit measurable absorption in the 290-380 nm
377 region (Colmenar et al., 2015).

378 For savannah grass, furanic compounds showed rapid early loss once UV light was switched on for photochemical
379 aging, and by 0.25 eqv. day of photochemical aging, EFs declined from 30.7 to 18.8 g kg⁻¹ in Exp. 2 (39% depletion,
380 min) and from 25.7 to 9.6 g kg⁻¹ in Exp. 7 (63% depletion, max). Phenolic compounds were depleted more strongly
381 from 5.7 to 2.4 g kg⁻¹ in Exp. 2 (58% depletion, min) and from 3.4 to 0.8 g kg⁻¹ in Exp. 7 (76% depletion, max)
382 during the same early decay (0.25 eqv. day) period. By 0.5 eqv. day of photochemical aging, >75% of furanic and



383 >80% of phenolic compounds were depleted across all the savannah grass experiments, with the greatest overall
 384 losses observed in Exp. 7. Oxygenated aromatics showed similar behavior, declining by ~77-81% by 0.5 eqv. day
 385 of photochemical aging with only 0.2 g kg⁻¹ remaining by the end of Exp. 7. The large reduction in furanic, phenolic
 386 and oxygenated aromatic compounds highlight the highly reactive nature of these species with OH.



387
 388 **Figure 2.** Chemical evolution of organic vapors is categorized by functional groups throughout aging in the smog
 389 chamber. X-axis shows equivalent aging time up to 0.5 eqv. day across experiments, Y-axis represents emission
 390 factors (EFs) in g of emission per kg of biomass fuel burnt. Aging time t=0 represents when UV light was switched
 391 on for photochemical aging experiments or when O₃ was injected for dark-aging experiments.

392
 393 Savannah wood experiments also showed ~70-80% depletion for furanic, phenolic and oxygenated aromatic
 394 compounds by 0.5 eqv. day of aging across all photochemical aging experiments, with the largest reductions
 395 observed in Exp. 8. For boreal forest surface fuel, only 21% (Exp. 12) and 29% (Exp. 20) of the furanic compounds
 396 remained by 0.5 eqv. day of aging. Phenolic compounds and oxygenated aromatics showed comparable depletions
 397 with larger reductions (~78%) in Exp. 12. ArHCs including benzene (C₆H₆, m/z 79.05), toluene (C₇H₈, m/z 93.07),
 398 xylenes/ethylbenzene (C₈H₁₀, m/z 107.08) declined, with overall reduction of ~33-45% for ArHCs for savannah
 399 fuels and >50% for boreal forest surface by 0.5 eqv. day of aging. Aromatic species are susceptible to multiple
 400 oxidation pathways and actively drive complex chemical reactions in the atmosphere, strongly governed by OH.



401 reactivity (Ziemann & Atkinson, 2012). C_xH_y compounds also substantially decayed by 65-76% across the biomass
402 fuels. Reductions in the EFs of N-containing compounds were also observed across different experiments. It is
403 important to note that in general, the variability in atmospheric precursor depletion dynamics is highly dependent
404 on differences in oxidant availability, their photochemical reactivity and the chemical composition of the emissions
405 (Georgopoulou et al., 2025; Henze et al., 2008; Liu et al., 2018; Ziemann & Atkinson, 2012).

406 Subcategories of certain oxygenated classes behaved differently when exposed to photochemical aging. E.g. the
407 EFs of compounds corresponding to the ‘carbonyl A’ group overall decreased by 40-48% for savannah fuels and
408 29-33% for boreal forest surface by 0.5 eqv. day with substantial reduction observed for some key carbonyl
409 compounds for e.g. crotonaldehyde (C_4H_5O , m/z 70.04), methacrolein or MVK (C_4H_6O , m/z 71.04) and acetic
410 anhydride ($C_4H_6O_3$, m/z 103.03) decaying by 55-83%, 47-66% and 30-53% across fuels, respectively. In contrast
411 to carbonyl A compounds, photooxidation led to ~3-5 fold higher EFs across fuels for certain acid compounds
412 from ‘carbonyl B’ for e.g. glycolic acid ($C_2H_4O_3$, m/z 77.02) and fumaric acid ($C_4H_4O_4$, m/z 117.01), with most of
413 the enhancement observed already by 0.25 eqv. day of aging. These C_2 - C_4 aliphatic oxygenates were also observed
414 in the day-time aged plume at an urban site several hours downwind of the wildfires in a previous study by (Liang
415 et al., 2022b). Toxicological evidence has identified gaseous carbonyl compounds as critical contributors to the
416 adverse biological effects of wood combustion emissions (Dilger et al., 2023), and short-lived unsaturated
417 carbonyls have been shown to drive cellular responses as toxic constituents (Han et al., 2020). Carbonyl A contains
418 unsaturated carbonyls being strong electrophiles, such as acrolein and redox-active quinones potentially inducing
419 oxidative stress, such as benzoquinone, whereas carbonyl B is more dominated by small acids. Given the steady
420 increase of carbonyl B and decrease of carbonyl A, both the inhalation hazard and risk concerning the compound
421 class of volatile carbonyls is reduced by atmospheric aging.

422 The enhancement of these secondary organic vapors belonging to the carbonyl B class, e.g. acetic acid ($C_2H_4O_2$,
423 m/z 61.02), succinic anhydride ($C_4H_4O_3$, m/z 101.02), pyruvic acid ($C_3H_4O_3$, m/z 89.02) and acetone (C_3H_6O , m/z
424 59.04), was concurrent with the decline in several reactive primary organic vapor classes, suggesting their potential
425 to act as precursors for secondary carbonyl production. Succinic anhydride ($C_4H_4O_3$), a compound with structural
426 similarity with maleic anhydride, is identified as an important secondary organic vapor formed from
427 multigenerational chemistry (Coggon et al., 2019). Previous studies have shown that secondary OVOCs were
428 generated as oxidation products of ArHCs, phenol and furans during aging experiments (Coggon et al., 2019; Liu
429 et al., 2019).

430 Photooxidation of toluene generates oligomeric oxygenated organic products and small dicarboxylic acids (Sato
431 et al., 2007; Zhang et al., 2024) and has been reported as a potential source of SOA in urban air (Sato et al., 2007).
432 Furans have further been identified as highly $OH\cdot$ -reactive BB organic vapors whose oxidation contributes to the
433 formation of secondary OVOCs, including anhydrides and small acids (Coggon et al., 2019). To understand the
434 role of such key precursors in secondary OVOCs formation, we performed the correlations analysis between
435 toluene or furan, and formic acid ($C_1H_2O_2$), glycolic acid ($C_2H_4O_3$), fumaric acid ($C_4H_4O_4$) and succinic anhydride
436 ($C_4H_4O_3$) mixing ratios for photochemical aging experiments (Figure S3).

437 Across all fuels, those OVOCs exhibited strong negative correlations with toluene and furan. Excluding an
438 anomalous boreal forest surface case on 2022-05-25 for succinic anhydride ($C_4H_5O_3$), R ranges for formic acid
439 were -0.96 to -0.48 / -0.96 to -0.48, glycolic acid were -0.99 to -0.87 / -1.00 to -0.95, fumaric acid were -0.98 to
440 -0.75 / -0.99 to -0.75, and succinic anhydride were -0.93 to -0.59 / -0.95 to -0.68 for toluene and furan,



441 respectively. Additionally, degradation of formed SOA can also act as a source for these and other volatile organic
442 acids (Malecha & Nizkorodov, 2016). O-containing compounds also showed distinct behavior based on the number
443 of carbon present, and compounds containing $C \geq 6$ showed a net decrease of 47-66% for savannah fuels and 35-
444 57% for boreal forest surface by 0.5 eqv. day of photochemical aging. On the other hand, O-containing compounds
445 containing $C < 6$ showed overall enhancement of 11-32% across photochemical aging experiments for savannah
446 fuels, except experiment 6 (no net change), and relatively higher 32-37% overall enhancement across
447 photochemical aging experiments for the boreal forest surface fuel. We compared the average total organic vapor
448 EFs for the fresh and aged emissions across different experiments. Although an increase in the average total organic
449 vapor EFs would be expected after photochemical aging due to the formation of certain oxygenated subclasses
450 (carbonyl B, O-containing compounds $C < 6$) from reactive primary organic vapors discussed above, the average
451 total organic vapor EFs after aging were reduced by 5-20% for savannah wood, and 22-32% for boreal forest
452 surface, while for savannah grass, it showed mixed trends with reduction of 27-34% in Exp. 1,2,7 and 18, while a
453 relative increase of ~25% in exp 3,5 and 6 with respect to their average total primary EFs. It is important to consider
454 that the wall losses of organic vapors to chamber walls can lead to a reduction in total organic vapor concentration,
455 while in parallel oxidation can transform compounds that were initially undetected by PTR-MS (e.g. alkanes) into
456 more oxygenated products that fall within the PTR-MS detection range, as opposite effect. Additionally, particle-
457 phase processes, such as condensation/evaporation and reactive uptake of gases can also influence the gas-phase
458 behaviour. A detailed analysis of SOA formation and multiphase processes will be addressed in a separate study.
459 In contrast to the prominent effect of photochemical aging, with rapid changes in the composition of organic vapors
460 in the chamber across all the photochemical aging experiments, the dark aging experiments of BB did not show
461 substantial changes. Phenolic compounds, which react rapidly with NO_3^- , showed negligible or only minor
462 reductions in EFs during dark aging experiments, similar to other organic vapor classes. This suggests that NO_3^-
463 formation was limited under our experimental conditions, and the observed evolution of organic vapors is
464 dominated by weak O_3 oxidation for dark aging experiments. This is in contrast with previous dark aging studies
465 of residential BB emissions where NO_3^- -driven oxidation resulted in substantial SOA production (Kodros et al.,
466 2022).
467 The difference in the behavior of organic vapors in different oxidation regimes is related to variability in
468 precursors' reactivity with the oxidants and their effective loss rates, which are governed by the corresponding
469 pseudo-first-order rate constants. Since most VOCs have higher reaction rates with OH^\cdot than with O_3 , it is expected
470 that the oxidation process in the chamber is mainly driven by OH^\cdot (Li et al., 2023). O_3 exhibits negligible reactivity
471 (Ziemann & Atkinson, 2012) with alkanes, other saturated VOCs and simple aromatics such as benzene and
472 alkylated benzene ($k \lesssim 10^{-23}$ – 10^{-20} $\text{cm}^3 \text{ molecule}^{-1} \text{ s}^{-1}$ at 298 K). Therefore, reactions with these compounds are
473 slow, and their lifetimes with respect to O_3 are orders of magnitude longer than their lifetime with respect to other
474 oxidants (Atkinson, 2000).
475 However, for BB-related ArHC such as styrene and unsaturated HCs, especially for many terpenes, O_3 can be an
476 important oxidant. A recent chamber study on BB emissions similarly showed that the reactions with OH^\cdot are the
477 dominant daytime oxidation pathway for most VOCs, while O_3 -induced oxidation was a minor consumption
478 mechanism for most species ($k_{\text{O}_3} = 10^{-17}$ – 10^{-22} $\text{cm}^3 \text{ molecule}^{-1} \text{ s}^{-1}$), with the main exception of monoterpenes and
479 their fragments, for which O_3 was important (Georgopoulou et al., 2025).



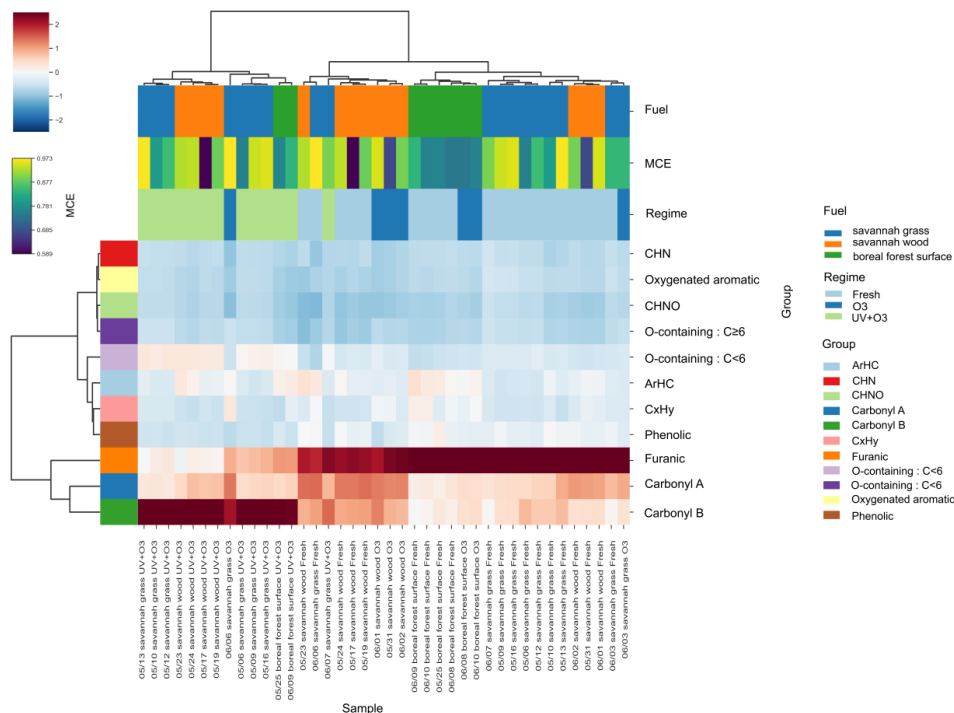
480 The relative share of each class (Figure S1) shows a compositional shift similar to that observed in the EF_s trends
481 discussed above. The relative share of classes in fresh emissions was compared to their relative share in different
482 aging emissions. For experiments later subjected to photochemical aging, the primary emissions were associated
483 with high emissions of carbonyl A, with a range of 20-28% relative share for savannah grass, 27-30% for savannah
484 wood and 15% for boreal forest surface. This was followed by furanic compounds with 25-44% relative share for
485 savannah grass, 16-21% for savannah wood and 25-27% for boreal forest surface. On exposure to photochemical
486 aging over 0.5 eqv. day, their relative share reduced to 10-30% for savannah grass, 9-11% for savannah wood and
487 17-18% for boreal forest surface while the relative share of carbonyl B increased from 6-7% to 12-15% for
488 savannah wood, from 4-7% to 8-17% for savannah grass and from 3-5% to 7-11% for boreal forest surface after
489 photooxidation. The relative share of O-containing compounds with C<6 nearly doubled across biomass fuels. For
490 dark aging experiments, the shifts for most compound classes were subtle, but the O-containing compounds with
491 C≥ 6 were found to be increasing on a relative scale from 7-13% to 13-34% for savannah grass, from 7-8% to 14-
492 19% for savannah wood, and from 7-8% to 11-14% for boreal forest surface.

493 3.3 Cluster analysis of organic vapor composition

494 We performed a cluster analysis to examine whether the broad organic vapor composition co-varies with
495 experimental factors (fuel, oxidation regime, MCE). A cluster map was constructed as shown in Figure 3 to
496 visualize samples and groups that share similar composition patterns. The cluster map comprises a central heatmap
497 accompanied by row and column dendrograms, which summarize similarities among variables (compound groups)
498 and observations (samples; date x fuel x oxidation regime), respectively.

499 The group-level mixing ratios were auto scaled by sample (column), thus, the heatmap colors indicated, within
500 each sample, relative enrichment/depletion of each compound group compared to that sample's mean. For both
501 row and column dendrogram in the cluster map, the cophenetic coefficients (*r*) were 0.88 (row) and 0.92 (column),
502 indicating good representation of the pairwise distances within variables and within observations and supporting
503 interpretation of the branch structure. On this relative composition scale, samples separated primarily by oxidation
504 regime, with UV+O₃ forming a distinct cluster in the dendrogram corresponding to a unique compositional regime,
505 while fresh and O₃ remained comparatively close. Regime centroids in the composition space supported this
506 interpretation (Fresh-O₃= 0.67, Fresh-UV+O₃=3.10, and O₃-UV+O₃=2.64).

507



508

509 **Figure 3.** Hierarchically clustered heatmap of standardized mean mixing ratios grouped by compound groups
 510 (rows) and regime-resolved samples (columns; date x fuel x regime), with row and column dendrograms
 511 summarizing similarities among compound groups and regime-resolved samples, respectively. Columns represent
 512 individual samples across fresh, dark aging (O₃) and photochemical aging (UV+O₃) regimes for savannah grass,
 513 savannah wood and boreal forest surface. Values are sample-standardized z-scores (each column z-scored to mean
 514 =0, SD=1), so heatmap colors indicate relative enrichment (red) or depletion (blue) of a compound group within
 515 that sample. Column color tracks denote fuel (biomass type), MCE (modified combustion efficiency, continuous
 516 gradient), and regime, while row colors indicate compound groups. Strongest effect in clustering of standardized
 517 compositions were observed for the factor Aging Regime, particularly between “UV+O₃” and “Fresh” / “O₃”,
 518 followed by Fuel but no apparent effect by MCE.

519 The influence of fuel was less evident than photochemical aging, nevertheless clear compositional fingerprints
 520 across regimes. Savannah wood and savannah grass clustered more closely together, while boreal forest surface
 521 fuel generally separated, indicating compositionally distinct behavior. The heatmap revealed fuel-specific
 522 fingerprints that persisted across regimes. In the sample-standardized (column-z-scored) composition space, boreal
 523 forest surface exhibited a furanic/aromatic-leaning profile with carbonyl depletion. Across regime averages,
 524 furanic (+0.44z), ArHC (+0.25z) were elevated, while carbonyl A (-0.33z) and B (-0.41z) were suppressed.



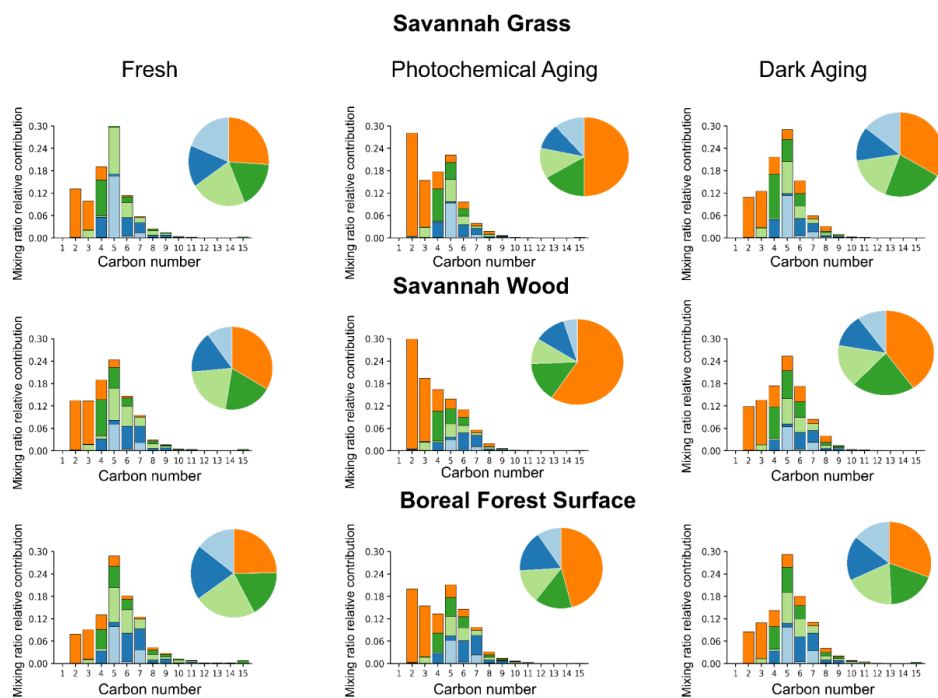
525 Savannah grass exhibited more oxygenated profile with elevated CHNO (+0.09z) and O-containing classes (+0.08-
526 0.10z), with carbonyl B (+0.24z) becoming prominent upon aging. Savannah wood was carbonyl rich and furanic-
527 poor, where carbonyl A (+0.38z) and B (+0.18z) were elevated while furanic compounds were reduced (-0.30z).
528 Thus, fuel sets the baseline composition while regime modulates it, notably UV+O₃ pushes the mixture towards
529 oxygenated functionality to a greater extent than O₃ alone, which is in line with the previous section.
530 PERMANOVA confirmed that oxidation regime explained most of the variance, whereas fuel played a smaller
531 role (Table S5). Across all samples, regime accounted for 73% of the variance in group-level composition ($R^2 =$
532 0.73, $F = 50.3$, $p = 0.001$), while fuel explained only 10% ($R^2 = 0.10$, $F = 2.08$, $p = 0.114$). Within each fuel, regime
533 remained highly significant and explained 73-96% of the variance ($R^2 = 0.73-0.96$, all $p = 0.001$ for savannah grass
534 and savannah wood, $p = 0.01$ for boreal forest surface), confirming that photochemical aging drives a coherent
535 compositional shift superimposed on fuel-specific baselines. Although there was a strong negative correlation
536 between MCE and absolute ΣEF_{VOC} (Vakkari et al 2025), it did not structure the relative composition space used
537 for clustering. A Mantel test showed no association between composition distance and $|\Delta MCE|$ ($\rho = -0.003$, $p =$
538 0.531).

539 3.4 Molecular-level characteristics

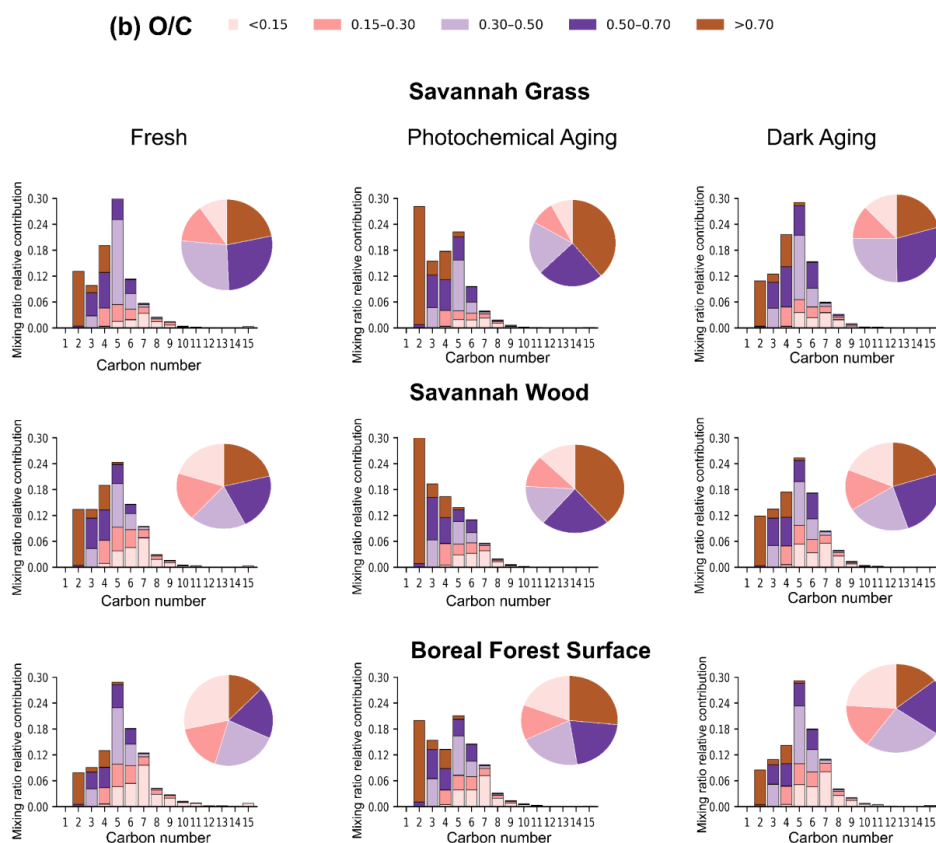
540 In Figure 4a, emitted compounds are separated according to their carbon number along the x-axis. The dominant
541 signals in organic vapors for savannah wood, savannah grass and boreal forest surface biomass fuels were
542 attributed to C₂-C₆ compounds, with dominant signals of C₅ compounds in fresh emissions. Compared to savannah
543 fuels, boreal forest surface showed more species with higher carbon numbers ($C \geq 9$). Under dark aging experiments,
544 the dominant signals were still concentrated within C₂-C₆ compounds across the biomass fuels. For photochemical
545 aging, the dominant signal of C₂ alone accounted for 28% of the total organic-vapor signal for savannah grass,
546 31% in savannah wood and nearly 20% in boreal forest surface. The lower carbon number shift after photochemical
547 aging indicates the rapid oxidation of condensable gases prior to those gases having time to condense on particles,
548 leading to fragmentation. However, other processes such as photolysis and heterogenous photooxidation of pre-
549 existing particle mass, leading to fragmentation and evaporation (Palm et al., 2016), may also result in the
550 production of small gas-phase molecules. The bin containing hydrogen-to-carbon ratios ($H/C > 1.7$) had the highest
551 contribution across biomass fuels, with the highest contribution in savannah wood ranging from 33% in primary
552 emission to 40% under dark aging and relatively higher, i.e. 59%, under photochemical aging. The addition of OH-
553 to aromatic rings and subsequent ring opening can increase H/C relative to primary emissions during gas-phase
554 oxidation (Liang et al., 2024). Oxygen-to-carbon ratios (O/C) presented in Figure 4b showed moderately oxidized
555 vapors (O/C = 0.5-0.7) contributed significantly to savannah fuels in both primary and dark aging experiments. In
556 contrast, boreal forest surface emissions showed a more substantial low-oxygen fraction (O/C < 0.15) in primary
557 (28%) and dark aging (24%), consistent with a high proportion of C_xH_y compounds. Photochemical aging led to
558 the formation of more oxygenated organic vapors with a high contribution of species with O/C > 0.7, reflecting
559 enhanced oxidative functionalization in savannah fuels (38%) and boreal forest surface biomass fuel (26%). Under
560 dark aging, however, a substantial low-oxygen fraction (O/C < 0.15) was retained. This contrast between
561 photochemical and dark aging is consistent with a chamber study by Cheung et al., 2025 which showed OH-driven
562 photooxidation produced much more oxidized aerosol than dark aging experiments.



(a) H/C <1.0 1.0-1.2 1.2-1.5 1.5-1.7 >1.7



563



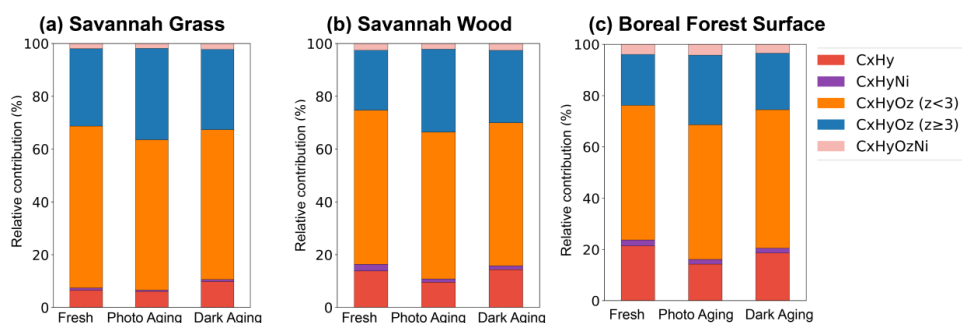
564

565 **Figure 4.** The average carbon distribution for savannah grass, savannah wood and boreal forest surface across
 566 fresh, photochemical aging and dark aging colored by (a) H/C and (b) O/C. The pie charts are the corresponding
 567 contributions by H/C and O/C ratios for each regime.

568 Based upon the elemental composition, molecular formulas were assigned to C_xH_y , $C_xH_yO_z$ ($z < 3$ and $z \geq 3$), $C_xH_yN_i$
 569 and $C_xH_yO_zN_i$ categories for their bulk-level characterization (Figure 5). In primary emissions, $C_xH_yO_z$ ($z < 3$)
 570 comprised of 53-61% of total mean mixing ratio (ppbv), followed by $C_xH_yO_z \geq 3$ (20-29%), C_xH_y (7-21%), and
 571 $C_xH_yN_i$ (1-3%) and $C_xH_yO_zN_i$ (2-4%). Photooxidation led to an increase in $C_xH_yO_z$ ($z \geq 3$) fraction from 23% in
 572 primary emission to 31% after photooxidation in savannah wood, 29-35% in savannah grass and 20 to 27% in
 573 boreal forest surface. High oxygen numbers in larger compounds relate to low volatilities that promote
 574 condensation on pre-existing surfaces, favor new particle formation and contribute to subsequent growth of newly
 575 formed particles, hence enhancing SOA formation (Ahern et al., 2019; Akherati et al., 2020; He et al., 2024). The
 576 mean mixing ratio distributions under fresh, photochemically aged and dark-aged conditions were largely centered
 577 at DBE values between 0 and 4. Photochemical aging shifted the distribution towards the lower DBE (particularly
 578 DBE =0-1) as presented in Figure S2. Organic vapors with a relatively low DBE are known to originate from
 579 oxidation of aliphatic precursors (An et al., 2024). High C_xH_y in boreal forest surface is consistent with findings
 580 discussed in previous section.



581

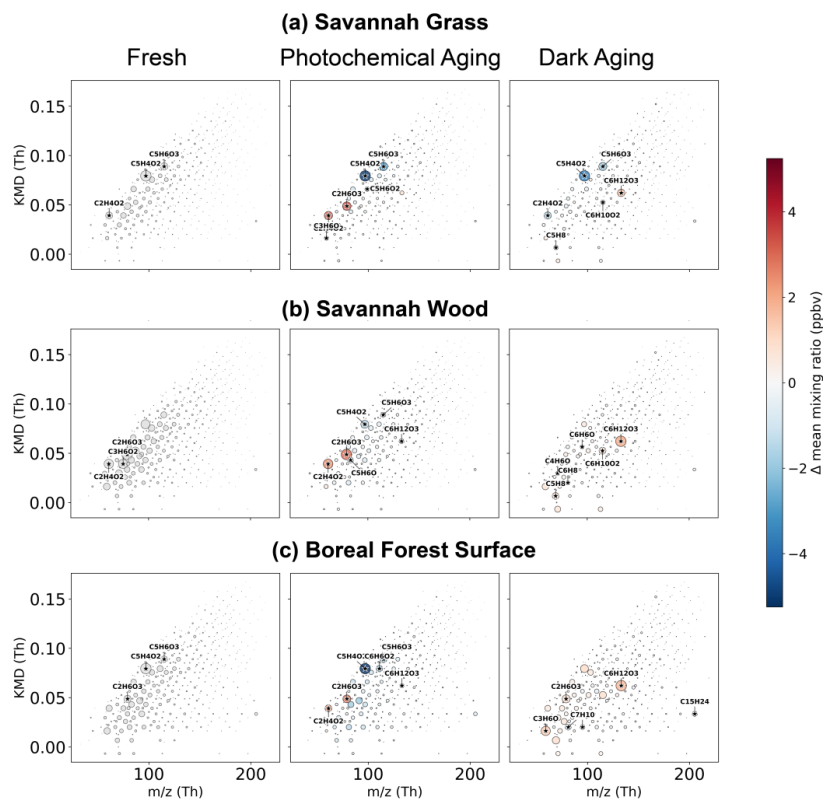


582

583 **Figure 5.** Stacked bar plots showing the relative contribution (%) of compound classes (C_xH_y, C_xH_yO_z (z < 3),
 584 C_xH_yO_z (z ≥ 3), C_xH_yN_i and C_xH_yO_zN_i) to the total mean mixing ratio (ppbv) for (a) savannah grass, (b) savannah
 585 wood and (c) boreal forest surface across fresh, photochemical aging and dark aging regimes.

586 Kendrick mass defect (KMD) plots (CH₂ base) for individual molecular formulas detected in fresh and aged
 587 emission for savannah grass, savannah wood and boreal forest surface show fresh emissions clustering at low-mid
 588 *m/z* with KMD ≈ 0.02–0.10, indicating dominance of lightly oxygenated CHO series immediately after emission
 589 (Figure 6). The most intense fresh formulas were C₅H₄O₂ (furfural; *m/z* 97.02), C₂H₄O₂ (acetic acid; *m/z* 61.02),
 590 C₅H₆O₃ (4-methoxy-2(5H)-furanone; *m/z* 115.040), C₃H₆O₂ (hydroxy acetone; *m/z* 75.045), and C₂H₆O₃ (*m/z*
 591 79.04). Horizontal alignment along the KMD band indicates a homologous series with shared backbones differing
 592 by CH₂ and was consistent across fuels. Dark aging produced modest increases for O-containing compounds with
 593 C ≥ 6, i.e. C₆H₁₂O₃ (*m/z* 133.08) across the biomass fuels, C₆H₁₀O₂ (*m/z* 115.076), and C₅H₈ hydrocarbon (e.g.
 594 isoprene or cyclopentene; *m/z* 69.07) for savannah fuels, alongside depletions of fresh dominant formulas such as
 595 C₅H₄O₂, C₅H₆O₃ and C₂H₄O₂. In boreal forest surface emission, C₃H₆O (acetone; 59.05) and C₂H₆O₃ (*m/z* 79.04)
 596 were enhanced. This pattern is consistent with selective ozonolysis of unsaturated olefinic and furanic precursors,
 597 where compounds containing C=C bonds are rapidly oxidized to a limited set of oxygenated products while others
 598 are consumed. O₃ preferentially reacts with C₆–C₇ olefinic hydrocarbons (e.g., C₆H₈, C₇H₁₀) and terpenoid
 599 fragments resulting in their depletion across fuels. Similarly, furanic compounds such as C₅H₄O₂ (furfural) and
 600 C₅H₆O₃ (furanone) also decreased through O₃ attack on the unsaturated furan ring.

601



602

603 **Figure 6.** Kendrick mass-defect (KMD) plots for savannah grass, savannah wood and boreal forest surface across
 604 fresh, dark aging (ΔO_3) and photochemical aging ($UV + \Delta O_3$). In fresh panel, marker size \propto to mean mixing ratio
 605 (ppbv), normalized within each biomass. In aging panels, marker size $\propto |\Delta| = ppbv_{aged} - ppbv_{fresh}$. Colors in aged
 606 panels encode the signed change on a global, symmetric scale: red = increase, blue = decrease (color intensity
 607 scales with $|\Delta|$). Top-changing species are indicated by black star markers and bold labels with a white outline.

608 Photooxidation ($UV + O_3$) drives larger, more coherent increases in mean mixing ratios centered at $m/z \sim 60-150$
 609 and $KMD \approx 0.04-0.10$, producing smaller, more oxygenated products across all fuels via a combination of
 610 fragmentation and functionalization reactions. Consistently, $C_2H_6O_3$ (m/z 79.040) and $C_2H_4O_2$ (acetic acid; m/z
 611 61.029) increased substantially. Enhancement for C_3H_6O (acetone; m/z 59.05) for savannah grass was also
 612 observed. The largest reduction occurred for $C_5H_4O_2$ (furfural; m/z 97.029) across the biomass fuels followed by
 613 $C_5H_6O_3$ (4-methoxy-2(5H)-furanone; m/z 115.040), indicating rapid conversion of primary C_5 -furanics compounds
 614 into smaller oxygenates. Prior smog chamber studies have examined oxidation of furan and methyl-substituted
 615 furans, and their reaction intermediates have been examined for SOA yields (Al Ali et al., 2024; Strollo & Ziemann,
 616 2013; Tajuelo et al., 2021; Yuan et al., 2017b). However, furanic compounds with additional oxygen-containing
 617 substituents have been examined far less, and in our study, they were rapidly transformed during photooxidation.
 618 The modest increase in some higher-mass oxygenates is consistent with limited functionalization, whereas the
 619 strong, coherent rise in mean mixing ratios of C_2 - C_3 oxygenates, alongside depletion of C_5 -furanic compounds,



620 suggests fragmentation-dominated chemistry. This fragmentation-dominated aging modulates radical (HO_x) and
621 O_3 chemistry and contributes to seed later SOA.

622 4 Conclusions

623 This work provides a detailed chemical characterization of BB organic vapors from a series of controlled laboratory
624 burns. We characterized organic vapor EFs from globally relevant savannah and European boreal forest surface
625 biomass fuels, using a high-resolution PTR-MS and investigated their transformation under photochemical and
626 dark aging experiments in a smog chamber. Primary emissions varied considerably between the biomass fuels,
627 with the highest average total organic vapor EF (160.8 g kg^{-1}) observed for European boreal forest surface biomass
628 and the lowest (69.1 g kg^{-1}) from savannah grass. These differences largely reflected variations in MCE together
629 with glowing combustion cases for savannah grass contributing to its lower overall EFs. In general, lower MCE
630 values resulted in higher emissions of organic vapors, consistent with previous BB studies. The total organic vapor
631 EFs reported here are generally higher than the values reported in previous studies (Gkatzelis et al., 2024; Koss et
632 al., 2018; Permar et al., 2021; Travis et al., 2023). This difference reflects the broader molecular coverage achieved
633 in the present study, where approximately 3–4 times more ions were considered.

634 Previous studies have emphasized the importance of VOCs emitted from BB in driving atmospheric oxidation
635 chemistry and secondary pollutant formation (Jin et al., 2026; Zhu et al., 2021). However, molecular-level
636 characterization of gas-phase organic compounds from savannah wildfires remains limited, and studies of boreal
637 BB have largely focused on North American ecosystems, with rare investigations on European boreal forest.

638 In the present study, primary emissions were dominated by small OVOCs such as furanic, carbonyl A and O-
639 containing compounds with $C < 6$ across the biomass fuels, with boreal forest surface exhibiting higher hydrocarbon
640 (C_xH_y) fractions and relatively more high-carbon species ($C \geq 9$). Across biomass fuels and regimes, $\text{C}_x\text{H}_y\text{O}_z$ ($z < 3$)
641 accounted for ~53–61% of the total organic vapor composition. Elemental and molecular composition analysis
642 revealed that fresh vapors were moderately oxidized, and under photooxidation of 0.5 eqv. day, the vapors shifted
643 towards higher O/C (> 0.70) with an increased fraction of $\text{C}_x\text{H}_y\text{O}_z$ ($z \geq 3$), alongside the formation of lower-carbon
644 products, indicating concurrent functionalization and fragmentation processes.

645 Photochemical aging produced pronounced compositional changes in organic vapors, whereas dark aging under
646 low- NO_x conditions resulted in minimal changes. This indicates that under our experimental conditions, OH-
647 driven photochemical oxidation exerted a more substantial influence on gas-phase organic composition than O_3 -
648 driven dark oxidation. Hierarchical clustering of relative composition reflected this regime-dependence, with
649 photochemical aging (UV+ O_3) forming a distinct cluster, while fresh and dark aging (O_3) conditions were relatively
650 similar. PERMANOVA showed a clear hierarchy of control on group-level organic vapor composition, with
651 oxidation regime being the dominant driver and accounting for 73% of the variance, whereas fuel played a
652 secondary role, and MCE exerted the weakest influence on the relative compositional structure. Under
653 photooxidation, major BB SOA precursors were substantially depleted. This included substantial loss of furanic,
654 phenolic and oxygenated aromatic compounds by 0.5 eqv. day of aging, with declines of ~70–82%, ~68–86% and
655 ~67–81% across the experiments, respectively. These losses underscore the need to account for non-traditional
656 precursors, particularly furanic and phenolic compounds in SOA models to more accurately represent SOA
657 formation from BB emissions. Subcategories of oxygenated compounds exhibited distinct evolutions in the
658 chamber, with pronounced increases observed for carbonyl B compounds such as glycolic acid ($\text{C}_2\text{H}_4\text{O}_3$, m/z



659 77.02), fumaric acid ($C_4H_4O_4$, m/z 117.01), acetic acid ($C_2H_4O_2$, m/z 61.02), succinic anhydride ($C_4H_4O_3$, m/z
660 101.02), and acetone (C_3H_6O , m/z 59.04), alongside increases in O- containing compounds with $C < 6$. This
661 coincided with a decline in primary reactive organic vapors, suggesting that they are likely precursors to secondary
662 oxygenate formation. Specifically, furan and toluene showed a strong negative correlation with carboxylic acids
663 and succinic anhydride, implying their role in the formation of secondary OVOCs.

664 Certain limitations should be considered when interpreting the results of these chamber experiments in context to
665 real atmospheric BB plumes. Chamber studies allow controlled investigation of aging processes but may not fully
666 capture the complexity of real atmospheric conditions. Variability in fuel composition and moisture content, plume
667 dilution rates, temperature, background aerosol concentrations, and potential chamber wall losses may affect the
668 emission chemistry. In addition, while PTR-MS provides high-sensitivity, real-time measurements of organic
669 vapors, it cannot reliably distinguish between structural isomers, which may introduce some uncertainties in
670 compound identification without complementary separation techniques. Another important aspect to consider is
671 that BB plumes in atmosphere undergo repeated cycles of daytime and nighttime oxidation during transport and
672 plumes may experience multi-day aging that can alter their chemical composition. Future studies should therefore
673 investigate longer-aging timescales and successive oxidation regimes, integrating field observations with
674 complementary analytical techniques to better capture the atmospheric evolution of BB plumes and improve their
675 representation in air quality and climate models.

676 Overall, the collective evidence from elemental ratios, carbon-number distributions, Kendrick mass-defect
677 analysis, and compositional clustering in this study converges on a coherent mechanistic picture that
678 photooxidation drives fragmentation-dominated chemistry (with some functionalization), transforming furanic and
679 aromatic precursors into smaller, more oxygenated, and potentially condensable products of decreased vapor
680 pressure. These results highlight the integral role of OH-driven photooxidation overcoming differences in BB
681 emission composition caused by fuel type and combustion conditions and provide critical insight into their
682 atmospheric evolution and molecular characteristics.

683

684 **Acknowledgements**

685 This project was supported by the Research Council of Finland (grant no 337550, 343359, 341597, 346371,
686 364229) and by the European Commission under the Horizon 2020 – Research and Innovation Framework
687 Programme, H2020-INFRAIA-2020-1, Grant Agreement No.: 101008004.

688 **Data availability**

689 The data is available from the data repository of the Finnish Meteorological Institute (FMI) at
690 <https://doi.org/10.57707/fmi-b2share.hvdp0-qtj25>.

691 **Competing interests**

692 The authors also have no competing interests to declare.

693 **Author contributions**

694 DS: data curation, formal analysis, investigation, visualization, writing – original draft preparation; LV: data
695 curation, formal analysis, investigation, writing – review and editing; MI: investigation, methodology; MS:
696 investigation, writing – review and editing; HC: supervision, writing – review and editing; SiSc: funding



697 acquisition, investigation, supervision, writing – review and editing; AB: investigation; IP: investigation, writing
698 – review and editing; KJ: investigation; KK: investigation, writing – review and editing; VL: investigation; PYP:
699 investigation; SJS: investigation, writing – review and editing; PGVZ: funding acquisition; AV: funding
700 acquisition, writing – review and editing; VV: conceptualization, data curation, funding acquisition, investigation,
701 project administration, supervision, writing – review and editing; OS: conceptualization, funding acquisition,
702 resources, supervision, writing – review and editing; RZ: funding acquisition, supervision, writing – review and
703 editing.

704

705 References

- 706 Ahern, A. T., Robinson, E. S., Tkacik, D. S., Saleh, R., Hatch, L. E., Barsanti, K. C., ... Donahue, N. M. (2019).
707 Production of Secondary Organic Aerosol During Aging of Biomass Burning Smoke From Fresh Fuels and
708 Its Relationship to VOC Precursors. *Journal of Geophysical Research: Atmospheres*, *124*(6), 3583–3606.
709 <https://doi.org/10.1029/2018JD029068>
- 710 Akagi, S. K., Craven, J. S., Taylor, J. W., McMeeking, G. R., Yokelson, R. J., Burling, I. R., ... Weise, D. R.
711 (2012). Evolution of trace gases and particles emitted by a chaparral fire in California. *Atmospheric*
712 *Chemistry and Physics*, *12*(3), 1397–1421. <https://doi.org/10.5194/acp-12-1397-2012>
- 713 Akagi, S. K., Yokelson, R. J., Wiedinmyer, C., Alvarado, M. J., Reid, J. S., Karl, T., ... Wennberg, P. O. (2011).
714 Emission factors for open and domestic biomass burning for use in atmospheric models. *Atmospheric*
715 *Chemistry and Physics*, *11*(9), 4039–4072. <https://doi.org/10.5194/acp-11-4039-2011>
- 716 Akherati, A., He, Y., Coggon, M. M., Koss, A. R., Hodshire, A. L., Sekimoto, K., ... Jathar, S. H. (2020).
717 Oxygenated Aromatic Compounds are Important Precursors of Secondary Organic Aerosol in Biomass-
718 Burning Emissions. *Environmental Science & Technology*, *54*(14), 8568–8579.
719 <https://doi.org/10.1021/acs.est.0c01345>
- 720 Al Ali, F., Cœur, C., Houzel, N., Genevray, P., Cazier, F., Cuisset, A., ... Romanias, M. N. (2024). Products and
721 yields for the NO₃ radical initiated atmospheric degradation of 2-methylfuran (2-MF, CH₃-C₄H₃O).
722 *Atmospheric Environment*, *319*, 120276. <https://doi.org/10.1016/j.atmosenv.2023.120276>
- 723 Allani, A., Bedjanian, Y., Papanastasiou, D. K., & Romanias, M. N. (2021). Reaction Rate Coefficient of OH
724 Radicals with *d*₉-Butanol as a Function of Temperature. *ACS Omega*, *6*(28), 18123–18134.
725 <https://doi.org/10.1021/acsomega.1c01942>
- 726 An, Z., Yin, R., Zhao, X., Li, X., Li, Y., Yuan, Y., ... Jiang, J. (2024). Molecular and seasonal characteristics of
727 organic vapors in urban Beijing: insights from Vocus-PTR measurements. *Atmospheric Chemistry and*
728 *Physics*, *24*(23), 13793–13810. <https://doi.org/10.5194/acp-24-13793-2024>
- 729 Anderson, M. J. (2001). A new method for non-parametric multivariate analysis of variance. *Austral Ecology*,
730 *26*(1), 32–46. <https://doi.org/10.1111/j.1442-9993.2001.01070.pp.x>
- 731 Anderson, M. J. (2017). Permutational Multivariate Analysis of Variance (<sc>PERMANOVA</sc>). *Wiley*



- 732 *StatsRef: Statistics Reference Online*, pp. 1–15. <https://doi.org/10.1002/9781118445112.stat07841>
- 733 Andreae, M. O. (2019). Emission of trace gases and aerosols from biomass burning – an updated assessment.
734 *Atmospheric Chemistry and Physics*, 19(13), 8523–8546. <https://doi.org/10.5194/acp-19-8523-2019>
- 735 Atkinson, R. (2000). Atmospheric chemistry of VOCs and NOx. *Atmospheric Environment*, 34(12–14), 2063–
736 2101.
- 737 Barmet, P., Dommen, J., DeCarlo, P. F., Tritscher, T., Praplan, A. P., Platt, S. M., ... Baltensperger, U. (2012).
738 OH clock determination by proton transfer reaction mass spectrometry at an environmental chamber.
739 *Atmospheric Measurement Techniques*, 5(3), 647–656. <https://doi.org/10.5194/amt-5-647-2012>
- 740 Bhattu, D., Zotter, P., Zhou, J., Stefenelli, G., Klein, F., Bertrand, A., ... Dommen, J. (2019). Effect of Stove
741 Technology and Combustion Conditions on Gas and Particulate Emissions from Residential Biomass
742 Combustion. *Environmental Science & Technology*, 53(4), 2209–2219.
743 <https://doi.org/10.1021/acs.est.8b05020>
- 744 Boby, L. A., Schuur, E. A. G., Mack, M. C., Verbyla, D., & Johnstone, J. F. (2010). Quantifying fire severity,
745 carbon, and nitrogen emissions in Alaska’s boreal forest. *Ecological Applications*, 20(6), 1633–1647.
746 <https://doi.org/10.1890/08-2295.1>
- 747 Brito, J., Rizzo, L. V., Morgan, W. T., Coe, H., Johnson, B., Haywood, J., ... Artaxo, P. (2014). Ground-based
748 aerosol characterization during the South American Biomass Burning Analysis (SAMBBA) field
749 experiment. *Atmospheric Chemistry and Physics*, 14(22), 12069–12083. <https://doi.org/10.5194/acp-14-12069-2014>
- 751 Bruns, E. A., El Haddad, I., Slowik, J. G., Kilic, D., Klein, F., Baltensperger, U., & Prévôt, A. S. H. (2016).
752 Identification of significant precursor gases of secondary organic aerosols from residential wood combustion.
753 *Scientific Reports*, 6(1), 27881. <https://doi.org/10.1038/srep27881>
- 754 Bruns, E. A., Slowik, J. G., El Haddad, I., Kilic, D., Klein, F., Dommen, J., ... Prévôt, A. S. H. (2017).
755 Characterization of gas-phase organics using proton transfer reaction time-of-flight mass spectrometry: fresh
756 and aged residential wood combustion emissions. *Atmospheric Chemistry and Physics*, 17(1), 705–720.
757 <https://doi.org/10.5194/acp-17-705-2017>
- 758 Cali Quaglia, F., Meloni, D., Muscari, G., Di Iorio, T., Ciardini, V., Pace, G., ... di Sarra, A. G. (2022). On the
759 Radiative Impact of Biomass-Burning Aerosols in the Arctic: The August 2017 Case Study. *Remote Sensing*,
760 14(2), 313. <https://doi.org/10.3390/rs14020313>
- 761 Calvert, J. G., Atkinson, R., Becker, K. H., Kamens, R. M., Seinfeld, J. H., Wallington, T. J., & Yarwood, G.
762 (2002). *The Mechanisms Of Atmospheric Oxidation Of Aromatic Hydrocarbons*.
763 <https://doi.org/10.1093/oso/9780195146288.001.0001>
- 764 Chen, L.-W. A., Verburg, P., Shackelford, A., Zhu, D., Susfalk, R., Chow, J. C., & Watson, J. G. (2010). Moisture
765 effects on carbon and nitrogen emission from burning of wildland biomass. *Atmospheric Chemistry and*
766 *Physics*, 10(14), 6617–6625. <https://doi.org/10.5194/acp-10-6617-2010>



- 767 Cheung, R. K. Y., Zhang, J., Wang, T., Kattner, L., Bogler, S., Puthussery, J. V., ... Modini, R. L. (2025). Online
768 Measurements during Simulated Atmospheric Aging Track the Strongly Increasing Oxidative Potential of
769 Complex Combustion Aerosols Relative to Their Primary Emissions. *Environmental Science & Technology*
770 *Letters*, 12(1), 64–72. <https://doi.org/10.1021/acs.estlett.4c00956>
- 771 Christian, T. J., Kleiss, B., Yokelson, R. J., Holzinger, R., Crutzen, P. J., Hao, W. M., ... Ward, D. E. (2003).
772 Comprehensive laboratory measurements of biomass-burning emissions: 1. Emissions from Indonesian,
773 African, and other fuels. *Journal of Geophysical Research: Atmospheres*, 108(D23).
774 <https://doi.org/10.1029/2003JD003704>
- 775 Coggon, M. M., Lim, C. Y., Koss, A. R., Sekimoto, K., Yuan, B., Gilman, J. B., ... Warneke, C. (2019). OH
776 chemistry of non-methane organic gases (NMOGs) emitted from laboratory and ambient biomass burning
777 smoke: evaluating the influence of furans and oxygenated aromatics on ozone and secondary NMOG
778 formation. *Atmospheric Chemistry and Physics*, 19(23), 14875–14899. <https://doi.org/10.5194/acp-19-14875-2019>
- 780 Colmenar, I., González, S., Jiménez, E., Martín, P., Salgado, S., Cabañas, B., & Albaladejo, J. (2015). UV
781 absorption cross sections between 290 and 380 nm of a series of furanaldehydes: Estimation of their
782 photolysis lifetimes. *Atmospheric Environment*, 103, 1–6. <https://doi.org/10.1016/j.atmosenv.2014.12.022>
- 783 Czech, H., Pieber, S. M., Tiitta, P., Sippula, O., Kortelainen, M., Lamberg, H., ... Zimmermann, R. (2017). Time-
784 resolved analysis of primary volatile emissions and secondary aerosol formation potential from a small-scale
785 pellet boiler. *Atmospheric Environment*, 158, 236–245. <https://doi.org/10.1016/j.atmosenv.2017.03.040>
- 786 Czech, H., Popovicheva, O., Chernov, D. G., Kozlov, A., Schneider, E., Shmargunov, V. P., ... Zimmermann, R.
787 (2024). Wildfire plume ageing in the Photochemical Large Aerosol Chamber (PHOTO-LAC).
788 *Environmental Science: Processes & Impacts*, 26(1), 35–55. <https://doi.org/10.1039/D3EM00280B>
- 789 Dai, J., Zhang, K., Feng, Y., Yi, X., Li, R., Xue, J., ... Li, L. (2025). Significant influence of oxygenated volatile
790 organic compounds on atmospheric chemistry: a case study in a typical industrial city in China. *Atmospheric*
791 *Chemistry and Physics*, 25(13), 7467–7484. <https://doi.org/10.5194/acp-25-7467-2025>
- 792 Decker, Z. C. J., Robinson, M. A., Barsanti, K. C., Bourgeois, I., Coggon, M. M., DiGangi, J. P., ... Brown, S. S.
793 (2021). Nighttime and daytime dark oxidation chemistry in wildfire plumes: an observation and model
794 analysis of FIREX-AQ aircraft data. *Atmospheric Chemistry and Physics*, 21(21), 16293–16317.
795 <https://doi.org/10.5194/acp-21-16293-2021>
- 796 Dilger, M., Armant, O., Ramme, L., Mülhopt, S., Sapcariu, S. C., Schlager, C., ... Weiss, C. (2023). Systems
797 toxicology of complex wood combustion aerosol reveals gaseous carbonyl compounds as critical
798 constituents. *Environment International*, 179, 108169. <https://doi.org/10.1016/j.envint.2023.108169>
- 799 EU-JRC. (2023). *Wildfires in the EU: 2022 was the second-worst year, a warning from a changing climate*.
800 Retrieved from [https://joint-research-centre.ec.europa.eu/jrc-news-and-updates/wildfires-eu-2022-was-](https://joint-research-centre.ec.europa.eu/jrc-news-and-updates/wildfires-eu-2022-was-second-worst-year-warning-changing-climate-2023-11-22_en)
801 [second-worst-year-warning-changing-climate-2023-11-22_en](https://joint-research-centre.ec.europa.eu/jrc-news-and-updates/wildfires-eu-2022-was-second-worst-year-warning-changing-climate-2023-11-22_en)
- 802 Fang, Z., Li, C., He, Q., Czech, H., Gröger, T., Zeng, J., ... Rudich, Y. (2021). Secondary organic aerosols



- 803 produced from photochemical oxidation of secondarily evaporated biomass burning organic gases: Chemical
804 composition, toxicity, optical properties, and climate effect. *Environment International*, 157, 106801.
805 <https://doi.org/10.1016/j.envint.2021.106801>
- 806 Fu, Y., Li, W., Manheim, J. M., Milton, J., Kilaz, G., & Kenttämä, H. I. (2022). Proton Affinities of Alkanes.
807 *Journal of the American Society for Mass Spectrometry*, 33(10), 1850–1857.
808 <https://doi.org/10.1021/jasms.2c00152>
- 809 Garofalo, L. A., Pothier, M. A., Levin, E. J. T., Campos, T., Kreidenweis, S. M., & Farmer, D. K. (2019). Emission
810 and Evolution of Submicron Organic Aerosol in Smoke from Wildfires in the Western United States. *ACS*
811 *Earth and Space Chemistry*, 3(7), 1237–1247. <https://doi.org/10.1021/acsearthspacechem.9b00125>
- 812 Gehm, C., Schnepel, K., Czech, H., Miersch, T., Ehlert, S., & Zimmermann, R. (2021). Hyper-fast gas
813 chromatography and single-photon ionisation time-of-flight mass spectrometry with integrated electrical
814 modulator-based sampling for headspace and online VOC analyses. *The Analyst*, 146(10), 3137–3149.
815 <https://doi.org/10.1039/D1AN00114K>
- 816 Georgopoulou, M. P., Florou, K., Matrali, A., Starida, G., Kaltsonoudis, C., Nenes, A., & Pandis, S. N. (2025).
817 Diurnal aging of biomass burning emissions: impacts on secondary organic aerosol formation and oxidative
818 potential. *Atmospheric Chemistry and Physics*, 25(22), 15835–15855. [https://doi.org/10.5194/acp-25-15835-](https://doi.org/10.5194/acp-25-15835-2025)
819 [2025](https://doi.org/10.5194/acp-25-15835-2025)
- 820 Gilman, J. B., Lerner, B. M., Kuster, W. C., Goldan, P. D., Warneke, C., Veres, P. R., ... Yokelson, R. J. (2015).
821 Biomass burning emissions and potential air quality impacts of volatile organic compounds and other trace
822 gases from fuels common in the US. *Atmospheric Chemistry and Physics*, 15(24), 13915–13938.
823 <https://doi.org/10.5194/acp-15-13915-2015>
- 824 Gkatzelis, G. I., Coggon, M. M., Stockwell, C. E., Hornbrook, R. S., Allen, H., Apel, E. C., ... Warneke, C. (2024).
825 Parameterizations of US wildfire and prescribed fire emission ratios and emission factors based on FIREX-
826 AQ aircraft measurements. *Atmospheric Chemistry and Physics*, 24(2), 929–956.
827 <https://doi.org/10.5194/acp-24-929-2024>
- 828 Gueneron, M., Erickson, M. H., VanderSchelden, G. S., & Jobson, B. T. (2015). PTR-MS fragmentation patterns
829 of gasoline hydrocarbons. *International Journal of Mass Spectrometry*, 379, 97–109.
830 <https://doi.org/10.1016/j.ijms.2015.01.001>
- 831 Han, J., Wang, S., Yeung, K., Yang, D., Gu, W., Ma, Z., ... Peng, H. (2020). Proteome-wide effects of naphthalene-
832 derived secondary organic aerosol in BEAS-2B cells are caused by short-lived unsaturated carbonyls.
833 *Proceedings of the National Academy of Sciences*, 117(41), 25386–25395.
834 <https://doi.org/10.1073/pnas.2001378117>
- 835 Hansel, A., Jordan, A., Holzinger, R., Prazeller, P., Vogel, W., & Lindinger, W. (1995). Proton transfer reaction
836 mass spectrometry: on-line trace gas analysis at the ppb level. *International Journal of Mass Spectrometry*
837 *and Ion Processes*, 149–150, 609–619. [https://doi.org/10.1016/0168-1176\(95\)04294-U](https://doi.org/10.1016/0168-1176(95)04294-U)
- 838 Hartikainen, A. H., Basnet, S., Yli-Pirilä, P., Ihalainen, M., Talvinen, S., Tissari, J., ... Sippula, O. (2024).



- 839 Resolving emission factors and formation pathways of organic gaseous compounds from residential
840 combustion of European brown coal. *Combustion and Flame*, 265, 113485.
841 <https://doi.org/10.1016/j.combustflame.2024.113485>
- 842 Hartikainen, A., Yli-Pirilä, P., Tiitta, P., Leskinen, A., Kortelainen, M., Orasche, J., ... Sippula, O. (2018). Volatile
843 Organic Compounds from Logwood Combustion: Emissions and Transformation under Dark and
844 Photochemical Aging Conditions in a Smog Chamber. *Environmental Science & Technology*, 52(8), 4979–
845 4988. <https://doi.org/10.1021/acs.est.7b06269>
- 846 Hatch, L. E., Yokelson, R. J., Stockwell, C. E., Veres, P. R., Simpson, I. J., Blake, D. R., ... Barsanti, K. C. (2017).
847 Multi-instrument comparison and compilation of non-methane organic gas emissions from biomass burning
848 and implications for smoke-derived secondary organic aerosol precursors. *Atmospheric Chemistry and
849 Physics*, 17(2), 1471–1489. <https://doi.org/10.5194/acp-17-1471-2017>
- 850 Hayden, K. L., Li, S.-M., Liggio, J., Wheeler, M. J., Wentzell, J. J. B., Leithead, A., ... Gentner, D. R. (2022).
851 Reconciling the total carbon budget for boreal forest wildfire emissions using airborne observations.
852 *Atmospheric Chemistry and Physics*, 22(18), 12493–12523. <https://doi.org/10.5194/acp-22-12493-2022>
- 853 He, Y., Zhao, B., Wang, S., Valorso, R., Chang, X., Yin, D., ... Donahue, N. M. (2024). Formation of secondary
854 organic aerosol from wildfire emissions enhanced by long-time ageing. *Nature Geoscience*, 17(2), 124–129.
855 <https://doi.org/10.1038/s41561-023-01355-4>
- 856 Henze, D. K., Seinfeld, J. H., Ng, N. L., Kroll, J. H., Fu, T.-M., Jacob, D. J., & Heald, C. L. (2008). Global
857 modeling of secondary organic aerosol formation from aromatic hydrocarbons: high- vs. low-yield pathways.
858 *Atmospheric Chemistry and Physics*, 8(9), 2405–2420. <https://doi.org/10.5194/acp-8-2405-2008>
- 859 Hobbs, P. V., Sinha, P., Yokelson, R. J., Christian, T. J., Blake, D. R., Gao, S., ... Pilewskie, P. (2003). Evolution
860 of gases and particles from a savanna fire in South Africa. *Journal of Geophysical Research: Atmospheres*,
861 108(D13). <https://doi.org/10.1029/2002JD002352>
- 862 Hodshire, A. L., Akherati, A., Alvarado, M. J., Brown-Steiner, B., Jathar, S. H., Jimenez, J. L., ... Pierce, J. R.
863 (2019). Aging Effects on Biomass Burning Aerosol Mass and Composition: A Critical Review of Field and
864 Laboratory Studies. *Environmental Science & Technology*, 53(17), 10007–10022.
865 <https://doi.org/10.1021/acs.est.9b02588>
- 866 Jaars, K., van Zyl, P. G., Beukes, J. P., Hellén, H., Vakkari, V., Josipovic, M., ... Hakola, H. (2016). Measurements
867 of biogenic volatile organic compounds at a grazed savannah grassland agricultural landscape in South
868 Africa. *Atmospheric Chemistry and Physics*, 16(24), 15665–15688. [https://doi.org/10.5194/acp-16-15665-
869 2016](https://doi.org/10.5194/acp-16-15665-2016)
- 870 Jaffe, D. A., & Wigder, N. L. (2012). Ozone production from wildfires: A critical review. *Atmospheric
871 Environment*, 51, 1–10. <https://doi.org/10.1016/j.atmosenv.2011.11.063>
- 872 Jensen, A. R., Koss, A. R., Hales, R. B., & de Gouw, J. A. (2023). Measurements of volatile organic compounds
873 in ambient air by gas-chromatography and real-time Vocus PTR-TOF-MS: calibrations, instrument
874 background corrections, and introducing a PTR Data Toolkit. *Atmospheric Measurement Techniques*,



- 875 *16*(21), 5261–5285. <https://doi.org/10.5194/amt-16-5261-2023>
- 876 Jin, L., Coggon, M. M., Permar, W., Juncosa Calahorrano, J. F., Palm, B. B., Gkatzelis, G. I., ... Hu, L. (2026).
877 Ozone photochemistry in fresh biomass burning smoke over the United States. *Science Advances*, *12*(6).
878 <https://doi.org/10.1126/sciadv.ads2157>
- 879 Junninen, H., Ehn, M., Petäjä, T., Luosujärvi, L., Kotiaho, T., Kostianen, R., ... Worsnop, D. R. (2010). A high-
880 resolution mass spectrometer to measure atmospheric ion composition. *Atmospheric Measurement*
881 *Techniques*, *3*(4), 1039–1053. <https://doi.org/10.5194/amt-3-1039-2010>
- 882 Kawamura, K., Okuzawa, K., Aggarwal, S. G., Irie, H., Kanaya, Y., & Wang, Z. (2013). Determination of gaseous
883 and particulate carbonyls (glycolaldehyde, hydroxyacetone, glyoxal, methylglyoxal, nonanal and decanal)
884 in the atmosphere at Mt. Tai. *Atmospheric Chemistry and Physics*, *13*(10), 5369–5380.
885 <https://doi.org/10.5194/acp-13-5369-2013>
- 886 Keywood, M., Kanakidou, M., Stohl, A., Dentener, F., Grassi, G., Meyer, C. P., ... Burrows, J. (2013). Fire in the
887 Air: Biomass Burning Impacts in a Changing Climate. *Critical Reviews in Environmental Science and*
888 *Technology*, *43*(1), 40–83. <https://doi.org/10.1080/10643389.2011.604248>
- 889 Kodros, J. K., Kaltsonoudis, C., Paglione, M., Florou, K., Jorga, S., Vasilakopoulou, C., ... Pandis, S. N. (2022).
890 Secondary aerosol formation during the dark oxidation of residential biomass burning emissions.
891 *Environmental Science: Atmospheres*, *2*(5), 1221–1236. <https://doi.org/10.1039/D2EA00031H>
- 892 Kodros, J. K., Papanastasiou, D. K., Paglione, M., Masiol, M., Squizzato, S., Florou, K., ... Pandis, S. N. (2020).
893 Rapid dark aging of biomass burning as an overlooked source of oxidized organic aerosol. *Proceedings of*
894 *the National Academy of Sciences*, *117*(52), 33028–33033. <https://doi.org/10.1073/pnas.2010365117>
- 895 Kolden, C. A., Abatzoglou, J. T., Jones, M. W., & Jain, P. (2024). Wildfires in 2023. *Nature Reviews Earth &*
896 *Environment*, *5*(4), 238–240. <https://doi.org/10.1038/s43017-024-00544-y>
- 897 Koss, A. R., Sekimoto, K., Gilman, J. B., Selimovic, V., Coggon, M. M., Zarzana, K. J., ... de Gouw, J. (2018).
898 Non-methane organic gas emissions from biomass burning: identification, quantification, and emission
899 factors from PTR-ToF during the FIREX 2016 laboratory experiment. *Atmospheric Chemistry and Physics*,
900 *18*(5), 3299–3319. <https://doi.org/10.5194/acp-18-3299-2018>
- 901 Köster, K., Kohli, J., Lindberg, H., & Pumpanen, J. (2024). Post-fire soil greenhouse gas fluxes in boreal Scots
902 pine forests—Are they affected by surface fires with different severities? *Agricultural and Forest*
903 *Meteorology*, *349*, 109954. <https://doi.org/10.1016/j.agrformet.2024.109954>
- 904 Krechmer, J., Lopez-Hilfiker, F., Koss, A., Hutterli, M., Stoermer, C., Deming, B., ... de Gouw, J. (2018).
905 Evaluation of a New Reagent-Ion Source and Focusing Ion–Molecule Reactor for Use in Proton-Transfer-
906 Reaction Mass Spectrometry. *Analytical Chemistry*, *90*(20), 12011–12018.
907 <https://doi.org/10.1021/acs.analchem.8b02641>
- 908 Kroll, J. H., & Seinfeld, J. H. (2008). Chemistry of secondary organic aerosol: Formation and evolution of low-
909 volatility organics in the atmosphere. *Atmospheric Environment*, *42*(16), 3593–3624.



- 910 <https://doi.org/10.1016/j.atmosenv.2008.01.003>
- 911 Kroll, J. H., Smith, J. D., Che, D. L., Kessler, S. H., Worsnop, D. R., & Wilson, K. R. (2009). Measurement of
912 fragmentation and functionalization pathways in the heterogeneous oxidation of oxidized organic aerosol.
913 *Physical Chemistry Chemical Physics*, *11*(36), 8005. <https://doi.org/10.1039/b905289e>
- 914 Lambe, A. T., Onasch, T. B., Croasdale, D. R., Wright, J. P., Martin, A. T., Franklin, J. P., ... Davidovits, P.
915 (2012). Transitions from Functionalization to Fragmentation Reactions of Laboratory Secondary Organic
916 Aerosol (SOA) Generated from the OH Oxidation of Alkane Precursors. *Environmental Science &*
917 *Technology*, *46*(10), 5430–5437. <https://doi.org/10.1021/es300274t>
- 918 Leskinen, A., Yli-Pirilä, P., Kuusalo, K., Sippula, O., Jalava, P., Hirvonen, M.-R., ... Lehtinen, K. E. J. (2015).
919 Characterization and testing of a new environmental chamber. *Atmospheric Measurement Techniques*, *8*(6),
920 2267–2278. <https://doi.org/10.5194/amt-8-2267-2015>
- 921 Lewis, A. C., Evans, M. J., Hopkins, J. R., Punjabi, S., Read, K. A., Purvis, R. M., ... Parrington, M. (2013). The
922 influence of biomass burning on the global distribution of selected non-methane organic compounds.
923 *Atmospheric Chemistry and Physics*, *13*(2), 851–867. <https://doi.org/10.5194/acp-13-851-2013>
- 924 Lewis, Alastair C., Carslaw, N., Marriott, P. J., Kinghorn, R. M., Morrison, P., Lee, A. L., ... Pilling, M. J. (2000).
925 A larger pool of ozone-forming carbon compounds in urban atmospheres. *Nature*, *405*(6788), 778–781.
926 <https://doi.org/10.1038/35015540>
- 927 Li, H., Almeida, T. G., Luo, Y., Zhao, J., Palm, B. B., Daub, C. D., ... Ehn, M. (2022). Fragmentation inside
928 proton-transfer-reaction-based mass spectrometers limits the detection of ROOR and ROOH peroxides.
929 *Atmospheric Measurement Techniques*, *15*(6), 1811–1827. <https://doi.org/10.5194/amt-15-1811-2022>
- 930 Li, H., Riva, M., Rantala, P., Heikkinen, L., Daellenbach, K., Krechmer, J. E., ... Bianchi, F. (2020). Terpenes and
931 their oxidation products in the French Landes forest: insights from Vocus PTR-TOF measurements.
932 *Atmospheric Chemistry and Physics*, *20*(4), 1941–1959. <https://doi.org/10.5194/acp-20-1941-2020>
- 933 Li, J., Xie, X., Li, L., Wang, X., Wang, H., Jing, S., ... Hu, J. (2022). Fate of Oxygenated Volatile Organic
934 Compounds in the Yangtze River Delta Region: Source Contributions and Impacts on the Atmospheric
935 Oxidation Capacity. *Environmental Science & Technology*, *56*(16), 11212–11224.
936 <https://doi.org/10.1021/acs.est.2c00038>
- 937 Li, K., Zhang, J., Bell, D. M., Wang, T., Lamkaddam, H., Cui, T., ... Prevot, A. S. H. (2024). Uncovering the
938 dominant contribution of intermediate volatility compounds in secondary organic aerosol formation from
939 biomass-burning emissions. *National Science Review*, *11*(3). <https://doi.org/10.1093/nsr/nwae014>
- 940 Li, R., Li, S., Jiang, X., Wu, Y., & Hu, K. (2024). Organic Vapors from Residential Biomass Combustion: Emission
941 Characteristics and Conversion to Secondary Organic Aerosols. *Atmosphere*, *15*(6), 692.
942 <https://doi.org/10.3390/atmos15060692>
- 943 Li, S., Liu, D., Wu, Y., Hu, K., Jiang, X., Tian, P., ... Zhao, D. (2023). Aging effects on residential biomass burning
944 emissions under quasi-real atmospheric conditions. *Environmental Pollution*, *337*, 122615.



- 945 <https://doi.org/10.1016/j.envpol.2023.122615>
- 946 Liang, C., Wang, S., Zhao, B., Xie, J., Li, Y., Feng, B., ... Hao, J. (2024). Secondary Organic Aerosol Formation
947 from the Photooxidation of Aromatic Ketone Intermediate Volatile Organic Compounds. *Environmental*
948 *Science & Technology*, 58(48), 21275–21285. <https://doi.org/10.1021/acs.est.4c05384>
- 949 Liang, Y., Stamatis, C., Fortner, E. C., Wernis, R. A., Van Rooy, P., Majluf, F., ... Goldstein, A. H. (2022).
950 Emissions of organic compounds from western US wildfires and their near-fire transformations. *Atmospheric*
951 *Chemistry and Physics*, 22(15), 9877–9893. <https://doi.org/10.5194/acp-22-9877-2022>
- 952 Liang, Y., Weber, R. J., Misztal, P. K., Jen, C. N., & Goldstein, A. H. (2022). Aging of Volatile Organic
953 Compounds in October 2017 Northern California Wildfire Plumes. *Environmental Science & Technology*,
954 56(3), 1557–1567. <https://doi.org/10.1021/acs.est.1c05684>
- 955 Liu, C., Chen, T., Liu, Y., Liu, J., He, H., & Zhang, P. (2019). Enhancement of secondary organic aerosol formation
956 and its oxidation state by SO₂ during photooxidation of 2-methoxyphenol. *Atmospheric Chemistry and*
957 *Physics*, 19(4), 2687–2700. <https://doi.org/10.5194/acp-19-2687-2019>
- 958 Liu, Q., Gao, Y., Huang, W., Ling, Z., Wang, Z., & Wang, X. (2022). Carbonyl compounds in the atmosphere: A
959 review of abundance, source and their contributions to O₃ and SOA formation. *Atmospheric Research*, 274,
960 106184. <https://doi.org/10.1016/j.atmosres.2022.106184>
- 961 Liu, T., Huang, D. D., Li, Z., Liu, Q., Chan, M., & Chan, C. K. (2018). Comparison of secondary organic aerosol
962 formation from toluene on initially wet and dry ammonium sulfate particles at moderate relative humidity.
963 *Atmospheric Chemistry and Physics*, 18(8), 5677–5689. <https://doi.org/10.5194/acp-18-5677-2018>
- 964 Malecha, K. T., & Nizkorodov, S. A. (2016). Photodegradation of Secondary Organic Aerosol Particles as a Source
965 of Small, Oxygenated Volatile Organic Compounds. *Environmental Science & Technology*, 50(18), 9990–
966 9997. <https://doi.org/10.1021/acs.est.6b02313>
- 967 Marques, M. M., Beland, F. A., Lachenmeier, D. W., Phillips, D. H., Chung, F.-L., Dorman, D. C., ... Guyton, K.
968 Z. (2021). Carcinogenicity of acrolein, crotonaldehyde, and arecoline. *The Lancet Oncology*, 22(1), 19–20.
969 [https://doi.org/10.1016/S1470-2045\(20\)30727-0](https://doi.org/10.1016/S1470-2045(20)30727-0)
- 970 Mason, S. A., Field, R. J., Yokelson, R. J., Kochivar, M. A., Tinsley, M. R., Ward, D. E., & Hao, W. M. (2001).
971 Complex effects arising in smoke plume simulations due to inclusion of direct emissions of oxygenated
972 organic species from biomass combustion. *Journal of Geophysical Research: Atmospheres*, 106(D12),
973 12527–12539. <https://doi.org/10.1029/2001JD900003>
- 974 McKeen, S. A., Wotawa, G., Parrish, D. D., Holloway, J. S., Buhr, M. P., Hübler, G., ... Meagher, J. F. (2002).
975 Ozone production from Canadian wildfires during June and July of 1995. *Journal of Geophysical Research:*
976 *Atmospheres*, 107(D14). <https://doi.org/10.1029/2001JD000697>
- 977 Müller, M., Anderson, B. E., Beyersdorf, A. J., Crawford, J. H., Diskin, G. S., Eichler, P., ... Wisthaler, A. (2016).
978 In situ measurements and modeling of reactive trace gases in a small biomass burning plume. *Atmospheric*
979 *Chemistry and Physics*, 16(6), 3813–3824. <https://doi.org/10.5194/acp-16-3813-2016>



- 980 Nguyen, D.-L., Czech, H., Pieber, S. M., Schnelle-Kreis, J., Steinbacher, M., Orasche, J., ... Zimmermann, R.
981 (2021). Carbonaceous aerosol composition in air masses influenced by large-scale biomass burning: a case
982 study in northwestern Vietnam. *Atmospheric Chemistry and Physics*, 21(10), 8293–8312.
983 <https://doi.org/10.5194/acp-21-8293-2021>
- 984 Pagonis, D., Selimovic, V., Campuzano-Jost, P., Guo, H., Day, D. A., Schueneman, M. K., ... Jimenez, J. L.
985 (2023). Impact of Biomass Burning Organic Aerosol Volatility on Smoke Concentrations Downwind of
986 Fires. *Environmental Science & Technology*, 57(44), 17011–17021. <https://doi.org/10.1021/acs.est.3c05017>
- 987 Palm, B. B., Campuzano-Jost, P., Ortega, A. M., Day, D. A., Kaser, L., Jud, W., ... Jimenez, J. L. (2016). In situ
988 secondary organic aerosol formation from ambient pine forest air using an oxidation flow reactor.
989 *Atmospheric Chemistry and Physics*, 16(5), 2943–2970. <https://doi.org/10.5194/acp-16-2943-2016>
- 990 Palm, B. B., Peng, Q., Fredrickson, C. D., Lee, B. H., Garofalo, L. A., Pothier, M. A., ... Thornton, J. A. (2020).
991 Quantification of organic aerosol and brown carbon evolution in fresh wildfire plumes. *Proceedings of the*
992 *National Academy of Sciences*, 117(47), 29469–29477. <https://doi.org/10.1073/pnas.2012218117>
- 993 Permar, W., Wang, Q., Selimovic, V., Wielgasz, C., Yokelson, R. J., Hornbrook, R. S., ... Hu, L. (2021). Emissions
994 of Trace Organic Gases From Western U.S. Wildfires Based on WE-CAN Aircraft Measurements. *Journal*
995 *of Geophysical Research: Atmospheres*, 126(11). <https://doi.org/10.1029/2020JD033838>
- 996 Pfister, G. G., Wiedinmyer, C., & Emmons, L. K. (2008). Impacts of the fall 2007 California wildfires on surface
997 ozone: Integrating local observations with global model simulations. *Geophysical Research Letters*, 35(19).
998 <https://doi.org/10.1029/2008GL034747>
- 999 Pospisilova, V., Lopez-Hilfiker, F. D., Bell, D. M., El Haddad, I., Mohr, C., Huang, W., ... Slowik, J. G. (2020).
1000 On the fate of oxygenated organic molecules in atmospheric aerosol particles. *Science Advances*, 6(11).
1001 <https://doi.org/10.1126/sciadv.aax8922>
- 1002 Reinecke, T., Leiminger, M., Jordan, A., Wisthaler, A., & Müller, M. (2023). Ultrahigh Sensitivity PTR-MS
1003 Instrument with a Well-Defined Ion Chemistry. *Analytical Chemistry*, 95(32), 11879–11884.
1004 <https://doi.org/10.1021/acs.analchem.3c02669>
- 1005 Rivera-Adorno, F. A., Tomlin, J. M., Lata, N. N., Azzarello, L., Robinson, M. A., Washenfelder, R. A., ... Laskin,
1006 A. (2025). Chemical Imaging of Atmospheric Biomass Burning Particles from North American Wildfires.
1007 *ACS ES&T Air*, 2(4), 508–521. <https://doi.org/10.1021/acsestair.4c00242>
- 1008 Rogers, H. M., Ditto, J. C., & Gentner, D. R. (2020). Evidence for impacts on surface-level air quality in the
1009 northeastern US from long-distance transport of smoke from North American fires during the Long Island
1010 Sound Tropospheric Ozone Study (LISTOS) 2018. *Atmospheric Chemistry and Physics*, 20(2), 671–682.
1011 <https://doi.org/10.5194/acp-20-671-2020>
- 1012 San-Miguel-Ayanz Durrant, T., Boca, R., Maianti, P., Libertà, G., JACOME, F.O., Branco, A., DE, R., Suarez-
1013 Moreno, M., Ferrari, D. and Roglia, E., J. (2023). Forest Fires in Europe, Middle East and North Africa 2022.
1014 *Publications Office of the European Union, Luxembourg.*



- 1015 Sato, K., Hatakeyama, S., & Imamura, T. (2007). Secondary Organic Aerosol Formation during the Photooxidation
1016 of Toluene: NO_x Dependence of Chemical Composition. *The Journal of Physical Chemistry A*, 111(39),
1017 9796–9808. <https://doi.org/10.1021/jp071419f>
- 1018 Schneider, E., Czech, H., Popovicheva, O., Chichayeva, M., Kobelev, V., Kasimov, N., ... Zimmermann, R. (2024).
1019 Mass spectrometric analysis of unprecedented high levels of carbonaceous aerosol particles long-range
1020 transported from wildfires in the Siberian Arctic. *Atmospheric Chemistry and Physics*, 24(1), 553–576.
1021 <https://doi.org/10.5194/acp-24-553-2024>
- 1022 Sekimoto, K., Koss, A. R., Gilman, J. B., Selimovic, V., Coggon, M. M., Zarzana, K. J., ... de Gouw, J. (2018).
1023 High- and low-temperature pyrolysis profiles describe volatile organic compound emissions from western
1024 US wildfire fuels. *Atmospheric Chemistry and Physics*, 18(13), 9263–9281. <https://doi.org/10.5194/acp-18-9263-2018>
- 1026 Simon, L., Gros, V., Petit, J.-E., Truong, F., Sarda-Estève, R., Kalalian, C., ... Favez, O. (2023). Two years of
1027 volatile organic compound online in situ measurements at the Site Instrumental de Recherche par
1028 Télédétection Atmosphérique (Paris region, France) using proton-transfer-reaction mass spectrometry. *Earth
1029 System Science Data*, 15(5), 1947–1968. <https://doi.org/10.5194/essd-15-1947-2023>
- 1030 Sinha, P., Hobbs, P. V., Yokelson, R. J., Bertschi, I. T., Blake, D. R., Simpson, I. J., ... Novakov, T. (2003).
1031 Emissions of trace gases and particles from savanna fires in southern Africa. *Journal of Geophysical
1032 Research: Atmospheres*, 108(D13). <https://doi.org/10.1029/2002JD002325>
- 1033 Sokal, R. R., & Rohlf, F. J. (1962). THE COMPARISON OF DENDROGRAMS BY OBJECTIVE METHODS.
1034 *TAXON*, 11(2), 33–40. <https://doi.org/10.2307/1217208>
- 1035 Stabbert, R., Dempsey, R., Diekmann, J., Euchenhofer, C., Hagemester, T., Haussmann, H.-J., ... Veltel, D. J.
1036 (2017). Studies on the contributions of smoke constituents, individually and in mixtures, in a range of in
1037 vitro bioactivity assays. *Toxicology in Vitro*, 42, 222–246. <https://doi.org/10.1016/j.tiv.2017.04.003>
- 1038 Stocker, M., Ladstädter, F., & Steiner, A. K. (2021). Observing the climate impact of large wildfires on
1039 stratospheric temperature. *Scientific Reports*, 11(1), 22994. <https://doi.org/10.1038/s41598-021-02335-7>
- 1040 Stockwell, C. E., Veres, P. R., Williams, J., & Yokelson, R. J. (2015). Characterization of biomass burning
1041 emissions from cooking fires, peat, crop residue, and other fuels with high-resolution proton-transfer-
1042 reaction time-of-flight mass spectrometry. *Atmospheric Chemistry and Physics*, 15(2), 845–865.
1043 <https://doi.org/10.5194/acp-15-845-2015>
- 1044 Strollo, C. M., & Ziemann, P. J. (2013). Products and mechanism of secondary organic aerosol formation from the
1045 reaction of 3-methylfuran with OH radicals in the presence of NO_x. *Atmospheric Environment*, 77, 534–543.
1046 <https://doi.org/10.1016/j.atmosenv.2013.05.033>
- 1047 Swap, R. J., Annegarn, H. J., Suttles, J. T., King, M. D., Platnick, S., Privette, J. L., & Scholes, R. J. (2003). Africa
1048 burning: A thematic analysis of the Southern African Regional Science Initiative (SAFARI 2000). *Journal
1049 of Geophysical Research: Atmospheres*, 108(D13). <https://doi.org/10.1029/2003JD003747>



- 1050 Tajuelo, M., Rodríguez, D., Rodríguez, A., Escalona, A., Viteri, G., Aranda, A., & Diaz-de-Mera, Y. (2021).
1051 Secondary organic aerosol formation from the ozonolysis and oh-photooxidation of 2,5-dimethylfuran.
1052 *Atmospheric Environment*, 245, 118041. <https://doi.org/10.1016/j.atmosenv.2020.118041>
- 1053 Ten Brink, P., Zádor, J., Turányi, T., Wirtz, K., Pilling, M. J., Kroll, J. H., ... Lelieveld, J. (2022). Essentials in
1054 modern HPLC separations. *Atmospheric Chemistry and Physics*, 11(1), 143686.
1055 <https://doi.org/10.1016/j.proci.2004.08.276>
- 1056 Tiitta, P., Leskinen, A., Hao, L., Yli-Pirilä, P., Kortelainen, M., Grigonyte, J., ... Sippula, O. (2016).
1057 Transformation of logwood combustion emissions in a smog chamber: formation of secondary organic
1058 aerosol and changes in the primary organic aerosol upon daytime and nighttime aging. *Atmospheric
1059 Chemistry and Physics*, 16(20), 13251–13269. <https://doi.org/10.5194/acp-16-13251-2016>
- 1060 Tkacik, D. S., Robinson, E. S., Ahern, A., Saleh, R., Stockwell, C., Veres, P., ... Robinson, A. L. (2017). A dual-
1061 chamber method for quantifying the effects of atmospheric perturbations on secondary organic aerosol
1062 formation from biomass burning emissions. *Journal of Geophysical Research: Atmospheres*, 122(11), 6043–
1063 6058. <https://doi.org/10.1002/2016JD025784>
- 1064 Travis, K. R., Crawford, J. H., Soja, A. J., Gargulinski, E. M., Moore, R. H., Wiggins, E. B., ... Perring, A. E.
1065 (2023). Emission Factors for Crop Residue and Prescribed Fires in the Eastern US During FIREX-AQ.
1066 *Journal of Geophysical Research: Atmospheres*, 128(18). <https://doi.org/10.1029/2023JD039309>
- 1067 Vakkari, V., Beukes, J. P., Dal Maso, M., Aurela, M., Josipovic, M., & van Zyl, P. G. (2018). Major secondary
1068 aerosol formation in southern African open biomass burning plumes. *Nature Geoscience*, 11(8), 580–583.
1069 <https://doi.org/10.1038/s41561-018-0170-0>
- 1070 Vakkari, V., Beukes, J. P., Josipovic, M., & van Zyl, P. G. (2020). Observations of ozone formation in southern
1071 African savanna and grassland fire plumes. *Atmospheric Environment*, 223, 117256.
1072 <https://doi.org/10.1016/j.atmosenv.2019.117256>
- 1073 Vakkari, V., Kerminen, V., Beukes, J. P., Tiitta, P., Zyl, P. G., Josipovic, M., ... Laakso, L. (2014). Rapid changes
1074 in biomass burning aerosols by atmospheric oxidation. *Geophysical Research Letters*, 41(7), 2644–2651.
1075 <https://doi.org/10.1002/2014GL059396>
- 1076 Wang, T., Zhang, J., Lamkaddam, H., Li, K., Cheung, K. Y., Kattner, L., ... Bell, D. M. (2025). Chemical
1077 characterization of organic vapors from wood, straw, cow dung, and coal burning. *Atmospheric Chemistry
1078 and Physics*, 25(4), 2707–2724. <https://doi.org/10.5194/acp-25-2707-2025>
- 1079 Warneke, C., Schwarz, J. P., Dibb, J., Kalashnikova, O., Frost, G., Al-Saad, J., ... Crawford, J. (2023). Fire
1080 Influence on Regional to Global Environments and Air Quality (FIREX-AQ). *Journal of Geophysical
1081 Research: Atmospheres*, 128(2). <https://doi.org/10.1029/2022JD037758>
- 1082 Whitman, E., Parisien, M.-A., Thompson, D. K., & Flannigan, M. D. (2019). Short-interval wildfire and drought
1083 overwhelm boreal forest resilience. *Scientific Reports*, 9(1), 18796. <https://doi.org/10.1038/s41598-019-55036-7>
1084



- 1085 Wolfe, G. M., Hanisco, T. F., Arkinson, H. L., Blake, D. R., Wisthaler, A., Mikoviny, T., ... Cohen, R. C. (2022).
1086 Photochemical evolution of the 2013 California Rim Fire: synergistic impacts of reactive hydrocarbons and
1087 enhanced oxidants. *Atmospheric Chemistry and Physics*, 22(6), 4253–4275. <https://doi.org/10.5194/acp-22-4253-2022>
1088
- 1089 Yazdani, A., Takahama, S., Kodros, J. K., Paglione, M., Masiol, M., Squizzato, S., ... Nenes, A. (2023). Chemical
1090 evolution of primary and secondary biomass burning aerosols during daytime and nighttime. *Atmospheric
1091 Chemistry and Physics*, 23(13), 7461–7477. <https://doi.org/10.5194/acp-23-7461-2023>
- 1092 Yokelson, R. J., Christian, T. J., Karl, T. G., & Guenther, A. (2008). The tropical forest and fire emissions
1093 experiment: laboratory fire measurements and synthesis of campaign data. *Atmospheric Chemistry and
1094 Physics*, 8(13), 3509–3527. <https://doi.org/10.5194/acp-8-3509-2008>
- 1095 Yokelson, R. J., Goode, J. G., Ward, D. E., Susott, R. A., Babbitt, R. E., Wade, D. D., ... Hao, W. M. (1999).
1096 Emissions of formaldehyde, acetic acid, methanol, and other trace gases from biomass fires in North Carolina
1097 measured by airborne Fourier transform infrared spectroscopy. *Journal of Geophysical Research:
1098 Atmospheres*, 104(D23), 30109–30125. <https://doi.org/10.1029/1999JD900817>
- 1099 Yuan, B., Koss, A. R., Warneke, C., Coggon, M., Sekimoto, K., & de Gouw, J. A. (2017). Proton-Transfer-
1100 Reaction Mass Spectrometry: Applications in Atmospheric Sciences. *Chemical Reviews*, 117(21), 13187–
1101 13229. <https://doi.org/10.1021/acs.chemrev.7b00325>
- 1102 Yuan, Y., Zhao, X., Wang, S., & Wang, L. (2017). Atmospheric Oxidation of Furan and Methyl-Substituted Furans
1103 Initiated by Hydroxyl Radicals. *The Journal of Physical Chemistry A*, 121(48), 9306–9319.
1104 <https://doi.org/10.1021/acs.jpca.7b09741>
- 1105 Zhang, B., Shen, Z., Yang, X., He, K., Huang, S., Wu, W., ... Cao, J. (2024). Primary and Secondary Emissions
1106 of Carboxylic Acids from Solid Fuel Combustion: Insight into the Source Markers and Secondary Formation
1107 Mechanism. *Environmental Science & Technology Letters*, 11(6), 580–585.
1108 <https://doi.org/10.1021/acs.estlett.4c00339>
- 1109 Zhao, B., Zhuang, Q., Shurpali, N., Köster, K., Berninger, F., & Pumpanen, J. (2021). North American boreal
1110 forests are a large carbon source due to wildfires from 1986 to 2016. *Scientific Reports*, 11(1), 7723.
1111 <https://doi.org/10.1038/s41598-021-87343-3>
- 1112 Zhong, Q., Schutgens, N., Veraverbeke, S., & van der Werf, G. R. (2024). Increasing aerosol emissions from boreal
1113 biomass burning exacerbate Arctic warming. *Nature Climate Change*, 14(12), 1275–1281.
1114 <https://doi.org/10.1038/s41558-024-02176-y>
- 1115 Zhu, B., Huang, X.-F., Xia, S.-Y., Lin, L.-L., Cheng, Y., & He, L.-Y. (2021). Biomass-burning emissions could
1116 significantly enhance the atmospheric oxidizing capacity in continental air pollution. *Environmental
1117 Pollution*, 285, 117523. <https://doi.org/10.1016/j.envpol.2021.117523>
- 1118 Ziemann, P. J., & Atkinson, R. (2012). Kinetics, products, and mechanisms of secondary organic aerosol
1119 formation. *Chemical Society Reviews*, 41(19), 6582. <https://doi.org/10.1039/c2cs35122f>